THESIS

A DIRECT-READING PARTICLE SIZER (DRPS) WITH ELEMENTAL COMPOSITION ANALYSIS

Submitted by

James Robert Sipich

Department of Mechanical Engineering

In partial fulfillment of the requirements

For the Degree of Master of Science

Colorado State University

Fort Collins, Colorado

Spring 2023

Master's Committee

Advisor: Azer P. Yalin

John Volckens
Christian L'Orange
Ellison Carter

ABSTRACT

A DIRECT-READING PARTICLE SIZER (DRPS) WITH ELEMENTAL COMPOSITION ANALYSIS

There is a lack of aerosol measurement technology capable of quantifying, in real-time, the size, concentration, and composition of large inhalable particles with an aerodynamic diameter larger than 20 µm. Aerosols of this size penetrate the upper respiratory system upon inhalation and present surface contamination hazards upon settling. The ability to obtain information on the composition of airborne particles is necessary to identify and control risks from exposure to potentially toxic materials, especially in the workplace. The objective of this work was to validate the performance of a prototype Direct-Reading Particle Sizer (DRPS) that counts and sizes particles via time-of-flight light scattering and determines single-particle elemental composition via Laser-Induced Breakdown Spectroscopy (LIBS). Counting, sizing, and spectral measurement efficiency were evaluated using test aerosols of multiple materials with diameters between 25 and 125 µm. Particle sizing results showed good agreement with optical microscopy images. The relationship between the median aerodynamic diameters measured by the DRPS time-of-flight and optical microscopy was linear (Deming regression slope of 0.998) and strongly correlated ($r^2 > 0.999$). The mean absolute difference between the median aerodynamic diameters measured by the instrument by time-of-flight and microscopy over all 8 test aerosol types was 0.9 µm with a mean difference in interquartile range of 1.9 µm. The prototype sensor uses an optical triggering system and pulsed Nd:YAG laser to generate a microplasma and ablate falling particles. Particle composition is determined based on collected emission spectra using a

real-time material classification algorithm. The accuracy of the composition determinations was validated with a set of 1480 experimental spectra from four different aerosol test materials. We have studied the effects of varying detection thresholds and find operating conditions with good agreement to truth values (F_1 score ≥ 0.9). Details of the analysis method, including subtracting the spectral contribution from the air plasma, are discussed. The time-of-flight aerodynamic diameter measurement and LIBS elemental analysis capabilities demonstrated by the DRPS provide a system capable of both counting, sizing, and identifying the composition of large inhalable particles.

TABLE OF CONTENTS

CHAPTER 1 – INTRODUCTION

1.1 Background & motivation

There is a lack of aerosol sampling technology capable of simultaneous real-time characterization of the size, concentration, and composition of inhalable particles greater than ~20 µm in diameter. Exposure to inhalable aerosols is common but challenging to quantify and inhalation of any airborne particle poses potential health hazards regardless of the chemical composition[1–3]. A particle's aerodynamic diameter (d_a) determines where it is most likely to deposit in the body with toxicity depending on the particle's chemical composition. For occupational exposure, airborne particles are often separated into size categories based on their aerodynamic diameter (d_a) – respirable ($d_a \leq 4$ µm), thoracic ($d_a \leq 10$ µm), and inhalable ($d_a \leq 100$ µm)[4,5]. However, particles larger than the upper size limit of the inhalable fraction (100 µm) do exist in some environments, with a reasonable probability of inhalation[6]. The inhalable fraction is based on the penetration of particles into the nose and mouth while breathing and aerosol research and instrumentation have primarily focused on detecting small (respirable and thoracic) particles due to their prevalence in almost all environments and the health hazards associated with their inhalation. Few particles larger than 20 µm will penetrate further than the larynx. Instead, large particles tend to deposit in the upper respiratory system due to their high inertia[4,7]. Potential health hazards associated with particle inhalation and deposition in the upper respiratory system include irritation and infection in the nasal mucous membrane, asthmatic responses, and sinonasal cancer[8,9]. Many of these particles are eventually swallowed (via deposition or mucociliary clearance) and therefore pose potential hazards to the gastrointestinal tract[10,11].

Occupational exposure limits are often based on mass concentration[12]. Since the mass of a particle with given density scales with the cube of its diameter (i.e. its volume), the presence of large particles in an environment can contribute substantially to the total aerosol mass concentration. Therefore, the permissible exposure limit for many toxic materials can potentially be exceeded by the contribution of a small number of large airborne particles. Further, identification of the composition of airborne particles is also important from the standpoint of hazard identification and risk assessment. Simply knowing mass concentration may not be sufficient to effectively evaluate or reduce exposure risk. The composition of particles in many occupational settings varies greatly and it is probable that some particle types will be inherently more toxic than others. For example, higher levels of exposure are permitted for aluminum or iron oxide dust (15 and 5 mg/m^3, respectively) than for known carcinogens like nickel (1 mg/m^3) or beryllium (5 $\mu g/m^3$)[12].

One of the limiting factors in furthering our understanding of inhalable aerosol exposure has been a lack of adequate measurement techniques — specifically, time-resolved determination of the count, size, and composition of particles. A common sampling methodology for characterizing large particles in occupational settings involves active sampling and collecting of particles onto filter media[13]. These samples are typically sent to an off-site lab for analysis. However, *post facto* analysis via inductively coupled plasma mass spectroscopy (ICP-MS) or similar processes is expensive, may take weeks to return the results[14,15] and cannot provide information on the timing and/or duration of exposure events. The delay in receiving results means that harmful exposure levels may continue to be present for weeks or months after assessment occurs. Time-resolved instrumentation capable of providing particle size information does exist; however, these instruments are typically not well suited for evaluating large diameter particles. Modern instrumentation such as Aerodynamic Particle Sizers (e.g. 3321, TSI Inc. Shoreview, MN) and

Optical Particle Counters (e.g. Dustdecoder 11-D, GRIMM Technik Ainring, Germany), are appropriate for both research purposes and hazard monitoring in the workplace; however, these instruments are typically limited to a maximum particle size of approximately 20 µm. The Aerosol Mass Spectrometer[16] is an advanced direct-reading instrument capable of measuring both size and composition of aerosols, but only for particles less than 1 µm. The difficulties in the detection and counting of large particles include the following: 1) inertial losses during inlet aspiration or subsequent transmission of the particle into the detection region of the instrument[17] or 2) the tendency towards detector saturation due to substantial scattering signals in optical systems[18].

There remains, therefore, a need for an instrument allowing real-time sizing and elemental composition for particles larger than 20 µm as part of aerosol hazard monitoring in the workplace. An instrument with the ability to determine the composition of large inhalable particles in real-time combined with a counting and sizing system, as we demonstrate, can support methods of rapid response and mitigation of hazardous airborne materials. The focus of this work details the design and testing of a direct-reading particle sizer (DRPS) that uses optical scattering signals and laser-induced breakdown spectroscopy (LIBS) to obtain direct time-resolved measurements of the aerodynamic diameter and elemental composition of large (~20 - 100+ µm) airborne particles.

1.2 Optical particle detection & measurement

1.2.1 Mie scattering

Optical particle counting instruments detect the presence of particles by measuring scattered light. An illumination source (typically laser light) is directed at a passing stream of aerosols and photons are scattered in all directions as particles transit the light beam. The amplitude and angular profile of the light scattering intensity is described by Mie scattering theory. The Mie theory is based on an exact solution of the Maxwell equations for the scattering of an electromagnetic wave by a

homogenous spherical obstacle and describes light scattered by aerosol particles with a diameter roughly equal to the wavelength of the incident light and larger[19]. The angular distribution of scattered light is described by Mie theory in terms of light intensity as a function of scattering angle θ, defined by the propagation direction of the incident beam. The intensity profile is symmetric about the transmission axis of the incoming light[20]. For particles much larger than the incident light source's wavelength, most scattered radiation is directed in the forward scattering direction (i.e., small values of θ) due to constructive interference and the forward lobe consists primarily of diffracted light[21]. A simplified example of the scattered intensity profile in a single plane for a large spherical particle is provided in Figure 1.1.

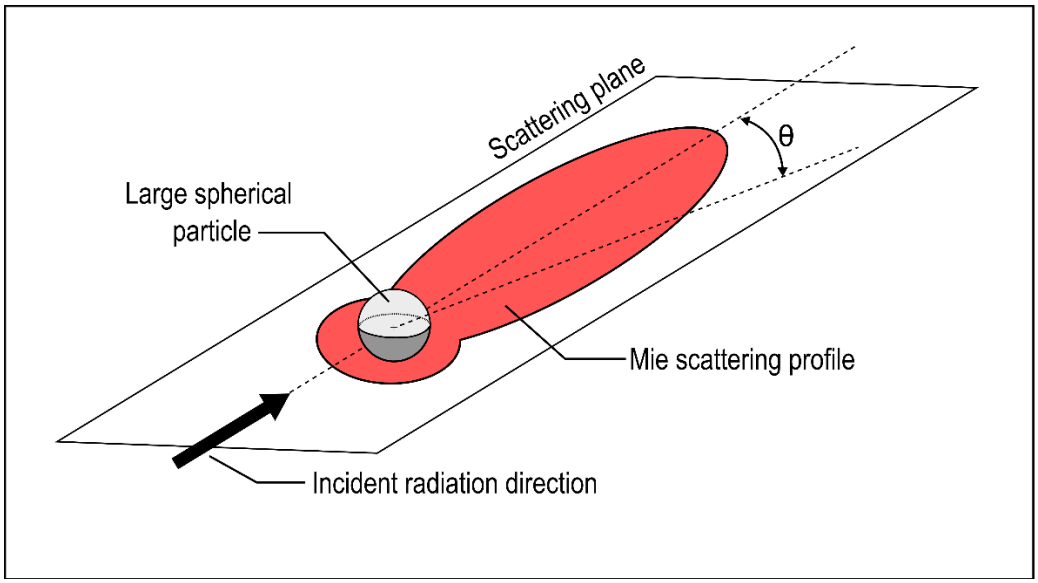

Figure 1.1: Illustrative diagram of scattered light intensity in the horizontal plane predicted by Mie scattering theory for a large spherical particle. Scattering angle θ is measured from the axis of incoming light propagation.

1.2.2 Optical particle counting

A photodetector placed off-axis of the illumination source can detect the scattered light and, therefore, the presence of a particle (or particles) within the incident beam. The detection and quantification of this scattered light is the primary mechanism used for particle detection by optical

particle counting instruments (OPC)[22,23]. In addition to counting particles, some more advanced optical particle counters also leverage the intensity profile given by Mie theory to determine particle size. Rather than a physical diameter, the intensity of the scattered light incident on an OPC's detector is a measure of the particle's optical diameter, which is greatly influenced by properties such as particle size, shape, and refractive index[24,25]. The optical diameter can be used to approximate a particle's true, physical diameter via calibration factors determined by measurement of uniform reference samples of known size for the specific optical scattering hardware and sampling scheme[26,27]. The OPC must be calibrated for a given particle material to reliably convert between optical diameter, physical diameter, or any other particle size measurement, such as aerodynamic diameter (defined below in Section 1.3), because the Mie scattering profile is highly dependent on a particle's complex index of refraction[28]. Thus, uncertainties develop when measuring heterogeneous samples with varying refractive indices.

1.3 Aerosol measurement fundamentals: aerodynamic diameter

This work builds upon the Portable Inhalable Particle Separator[29] to perform particle sizing based on a particle's terminal settling velocity (V_{TS}), the constant velocity achieved when drag and gravitational forces are in equilibrium[23]. The measurement of terminal settling velocity allows for the calculation of aerodynamic diameter (d_a):

$$V_{TS} = \begin{cases} \frac{\rho_0 d_a^2 g C_c}{18\eta} & Re < 1 \\ \left(\frac{\eta}{\rho_g d_a}\right) \exp(-3.07 + 0.9935J - 0.0178J^2) & 1 \leq Re \leq 1000 \\ where\ J = \ln\left(\frac{4\rho_0 \rho_g d_a^3 g}{3\eta^2}\right) & \end{cases} \quad (1.1)$$

where ρ_0 is the standard particle density (1000 kg/m^3), g is the acceleration due to gravity, C_c is the slip correction factor (C_c = 1 for particles >20 µm), η and ρ_g are the dynamic viscosity and

density of the surrounding gas, respectively. The aerodynamic diameter is the diameter of a spherical particle of standard density with equal settling velocity as the particle in question. It defines the aerodynamic properties of the particle necessary for characterizing filtration and respiratory deposition. The relationship between settling velocity and aerodynamic diameter Eqn. (1.1)[23] takes on a different functional form depending on the particle Reynolds number (Re). There is a theoretical basis for the relationship between particle velocity and particle size based on the Navier-Stokes equation when in the Stokes regime (Re < 1). However, at Reynolds numbers greater than 1, the assumptions made in the Stokes regime are no longer valid, and an empirical solution based on experimentation is used in the transition region ($1 \leq$ Re ≤ 1000). Depending on environmental conditions, the boundary between Stokes and transitional flow is typically reached for particle settling at aerodynamic diameters of approximately 80 µm and larger.

The aerodynamic diameter can be related to the spherical equivalent diameter (d_{eq}), which is defined as the diameter of a sphere having equal volume as a "standard" particle:

$$d_a = d_{eq}\sqrt{\frac{\rho_p}{\rho_0 \chi}} \tag{1.2}$$

Where χ is the dimensionless dynamic shape factor, ρ_p is the bulk density of the particle, and ρ_0 is the standard density (1000 kg/m^3). Irregular and nonspherical particles experience more drag than spherical particles with the same volume or mass because of their increased surface area. The shape factor (χ) is defined as the ratio of the drag force on a particle to the drag force on a sphere with equivalent volume, when both particles are moving with the same velocity (relative to the surrounding gas). Therefore, the dynamic shape factor depends on particle morphology, surface condition, and flow regime. Note that Eqn. (1.2) only applies in the continuum regime (Knudsen

number < 0.01) which typically corresponds to particles larger than ~13 µm at standard ranges of environmental conditions [23,30].

1.4 Laser-Induced Breakdown Spectroscopy (LIBS)

1.4.1 LIBS overview

To obtain direct, time-resolved elemental composition data, we build upon past work employing laser-induced breakdown spectroscopy (LIBS) to analyze particles[31–33]. The LIBS technique involves focusing a high-power laser pulse onto a sample to ablate material and then analyze the spectral content of light emitted from the resulting laser-induced microplasma[34]. The collected spectra provide a way to determine the elemental composition of a sample because each constituent element emits light at different characteristic wavelengths depending on its energy level structure. Extensive past research has examined how the mass of ablated material, its composition, and the position of the sample relative to the center of the plasma affect the spectral features of the collected LIBS signal[35,36]. In the present work, LIBS is used to analyze airborne particles as they settle *in situ*. Such an approach requires spatial and temporal overlap of the transient laser plasmas with the relatively small moving particles. The aspects of LIBS analysis that make it advantageous for a mobile, real-time aerosol sampling instrument are that the necessary components occupy little space, a laser plasma can be easily generated in small, enclosed areas, and a usable signal can be obtained by the ablation of only a few nanograms of material[34]. Furthermore, other spectroscopic techniques that are traditionally used on aerosol samples such as ICP-MS require a pre-prepared sample that is often dispersed with a nebulizer[37] for subsequent offline analysis of particle composition. Compositional analysis using LIBS, however, requires no sample preparation and can be performed in situ.

A laser-plasma spark is formed in a gas—in this application, the ambient room air—when the density of free electrons and ionized gas molecules is sufficiently high to induce breakdown[38]. For LIBS, free electrons are produced through avalanche and multiphoton ionization. Free electrons gain energy from the laser pulse and through electron-photon-ion collisions (inverse bremsstrahlung), further ionizing the gas and eventually forming a plasma. At the earliest stages of the plasma lifetime, the emitted light is dominated by continuum emission from photons produced by free-free and free-bound (recombination) electronic transitions. This creates broadband "white" light that contains no useful spectral information for LIBS. As the plasma decays, the continuum emission background signal is reduced, and photons are emitted primarily by atoms and simple molecules. These bound-bound electronic transitions provide the signals of interest used to identify the elemental composition of the plasma in LIBS. Time-gated spectrometer detectors have been used for LIBS to collect light in only the later stages of plasma decay and reduce the signal noise produced by continuum emission[34,39]. A time-gated detector has not been employed for the work discussed in this paper. Instead, the light emitted by the plasma over its entire lifetime is collected and continuum emission is present in all LIBS spectra and is suppressed by subtraction of reference spectra. The removal of continuum emission from the data as a post-processing step rather than precise timing of the signal acquisition allows for a comparatively low-cost spectrometer to be used in the DRPS prototype.

Photons emitted as excited electrons relax to lower energy states within the decaying plasma are recorded in the LIBS signal as narrow peaks at specific wavelengths depending on the energy structure of the atom in the form of emission lines. The height and width of these peaks are influenced by many factors, including the light collection and dispersion hardware as well as the concentration of a particular elemental species within the plasma[34,40]. The central wavelength of

each peak is determined by the frequency of photons emitted by bound-bound electronic transitions. The atomic spectral database compiled by the National Institute of Standards and Technology (NIST) contains data for energy level structure and radiative transitions for all elemental species[41]. Comparing the wavelengths of the detected lines against this database allows the identification of species present within the sample.

The current iteration of the DRPS is focused on qualitative material identification rather than quantitative measurement (i.e., the mass or concentration or a particular element), though quantitative LIBS on aerosol samples has been demonstrated in the past[42]. The primary factor in this work limiting the ability for quantitative measurements is particle size. The largest particle that will be completely vaporized by a LIBS plasma is in the range of 2-10 μm, depending on sample composition and laser parameters[43,44]. When a particle is not completely ablated by the plasma, as is the case for our size range of interest, the LIBS signal is no longer dependent on the particle mass[45] and the analyte measured in the collected spectrum may not be representative of the entire particle for a non-homogenous sample. Additionally, variability in particle position relative to the plasma and the test aerosol dispersion methodology cause difficulty introducing a known mass of analyte into the plasma for the purpose of constructing calibration curves.

A portable sampling device capable of real-time qualitative material identification of large particles could be a valuable tool for aerosol source apportionment. When a source apportionment study is conducted, the first step is sampling. The larger the size range of measured particles in the sampling step, the more complete and comprehensive the study results. Therefore, capturing particles in the > 20 μm size range is preferable and the DRPS could be used in combination with other instrumentation to get a complete picture of the ambient aerosol. Elemental composition analysis of the collected samples is often the next step in source apportionment. A common

methodology involves the use of receptor models, which infer contributions from different aerosol source types using multivariate measurements of particle composition and concentration taken at multiple locations, often using a chemical tracer for certain sources[46]. Compositional analysis for source apportionment is typically performed via X-ray fluorescence (XRF) spectroscopy. The advantage of XRF over many other analytical techniques such as ICP-MS is that it is typically non-destructive, requires no sample preparation and allows simultaneous analysis of multiple elements[47]. These advantageous features, however, also apply to laser-induced breakdown spectroscopy.

1.4.2 Material identification via LIBS

Material identification with LIBS most commonly uses relatively large, stationary solid samples and repeat (often 100s-1000s of laser shots) measurements to improve signal-to-noise ratios, including the possibility of moving the beam sample location throughout the measurement to achieve a more representative measurement of the overall sample[34]. Elemental analysis of aerosol samples using LIBS has also been demonstrated, also typically with stationary samples, where multiple approaches can be used to immobilize the particles, including collection on filters[48], on a charged needle[49], or trapping by an electrodynamic balance[50,51]. Although trapping single particles can be advantageous in some cases, we follow an approach in which particles settle through the instrument under the influence of only gravity. The falling particles carry information on their aerodynamic diameter (based on settling velocity), allowing us to perform both counting (with Mie scattering) and real-time composition measurements via LIBS. There have been several demonstrations of LIBS methods based on free-firing (untriggered) lasers aimed at moving aerosol streams; however, sampling rates (i.e., the probability of actually hitting a particle) were limited to only ~1-5%[52,53]. When the concentration of particles passing through the measurement volume

is high, a particle hit rate of <10% can still provide acceptable sampling rates. However, the number concentration (particle count per unit volume) of particles with da > 20 µm is typically orders of magnitude lower than that of small particles. Thus, an instrument aimed at characterizing large particles would require a higher probability of successful particle ablation. Performing LIBS on individual moving particles adds complexity in terms of requiring precise overlap of the particle and laser plasma in both time and space. There have been limited reports in the literature of such approaches. Tjarnhage et al. use an optical Mie scattering triggering scheme similar to the one described in this work (but with an aerosol concentrator at the inlet) and achieve single particle sampling rates up to 70%[54].

A challenge in LIBS analysis, particularly prevalent in sampling freefalling particles, is the necessity to discriminate between spectral features resulting from the ablation of the analyte particle versus the surrounding matrix, i.e., accompanying optical emission from the surrounding air. There can be more subtle "matrix effects", for example radiative or chemical coupling between the plasma due to the air and the particle, which influences the overall spectral features. These effects tend to be stochastic depending on overlap between the illuminating laser pulse and particle. Note that in our regime of laser pulse energy and particle size, the fraction of each particle that gets ablated by the laser-induced microplasma is small[52,55]. Because large particles are not completely vaporized by the plasma, the intensity of the resulting spectral emission lines is influenced primarily by the location of the particle relative to the plasma (i.e., the amount of plasma-particle overlap) rather than the particle size or the volume of the analyte in the whole particle. A related analysis challenge is the temporal evolution of plasma light. At the earliest stages of the plasma lifetime, the emitted light is dominated by broadband continuum emission, which is generally not useful for line-based spectral identification[34]. Subsequently, as the plasma

decays and the effect of continuum emission reduces, photons are emitted primarily by line emission (between bound states of the constituent atoms or ions), allowing the determination of elemental composition. Spectrometers with time-gated detection can be used to collect LIBS light only in the later stages of plasma decay as a means to reduce the contribution of the early-time continuum emission[34,56]; however, we do not follow such an approach owing to our interest in simpler, less expensive setups. Instead, we use a method based on measuring and subtracting reference spectra containing the continuum emission. Common approaches to mitigate the influence of continuum emission and/or matrix effects involve using intensity thresholds (relative to the baseline) to qualify individual spectral peaks. The thresholds can be adaptive based on background noise levels and peak intensities[52,57,58] or standard deviations of detector counts[59–61].

1.5 Thesis objectives and outline

The overarching objective of the present work is to develop and test a prototype aerosol sampling instrument capable of characterizing the size and composition of large (>20 μm) airborne particles to support aerosol research and occupational hazard monitoring. We aim to create a compact device that makes direct, near real-time measurements of settling particles to provide temporal and spatial information about aerosol concentration, size, and composition. To achieve our overall goal, we have a series of specific objectives related to validating and quantifying the performance of the prototype DRPS in the following areas:

- Detection and counting of particles with aerodynamic diameters greater than 20 μm
- Direct, single-particle measurement of aerodynamic diameter based on settling velocity
- Ablation of settling particles by a laser-induced microplasma
- Classification of aerosol composition and detection of “missed” particles by automated analysis of emission spectra

The ability of the prototype device to perform accurate particle characterization—both aerodynamic diameter and elemental composition—is validated in the laboratory by dispersing and measuring test aerosols of varying size, shape, and material. The measurements of aerodynamic diameter made by the device are compared against size distributions obtained by optical microscopy for agreement. A spectral processing and material classification method is developed to detect emission from particulate matter in the laser-induced plasma and identify the constituent elements.

The remainder of this thesis is as follows. Chapter 2 discusses the experimental hardware and setup used throughout this work and details of the test aerosol samples. The aerodynamic diameter measurement methods and a summary of experimental particle sizing results is presented in Chapter 3. The level of agreement between the two particle sizing methods (microscopy and the instrument) is analyzed and opportunities for optimization of the design of the device are discussed. Chapter 4 contains details of the LIBS signal classification algorithm and information on the set of experimental spectra used to evaluate the performance. An adaptive threshold on detectable peak intensity for material classification is introduced and an optimal range of threshold values based on the test spectra is presented. Opportunities for optimization of the spectral analysis algorithm, as well as LIBS system hardware, are discussed at the end of the Chapter 4. The concluding chapter briefly summarizes the results of the particle sizing and elemental composition analysis validation testing and presents potential opportunities for future work. Some of the materials presented in this thesis have also been published in *A direct-reading particle sizer with elemental composition analysis for large inhalable particles*[62] and *In-Situ Elemental Composition Analysis of Large Inhalable Aerosol Using Laser Induced Breakdown Spectroscopy*[63].

2.1 Summary

A Direct-Reading Particle Sizer (DRPS) to determine the count, size, and elemental composition of large particles (~20-100 μm) was developed and evaluated in the laboratory. Particles are counted and sized based on their time-of-flight as they settle through a pair of vertically 785 nm continuous-wave diode laser beams. Particles passing the 2nd (lower) beam trigger a LIBS laser pulse directed at the particle location used to determine elemental composition. A schematic of the DRPS is provided in Figure 2.1 and an overview of the experiment setup in Figure 2.2.

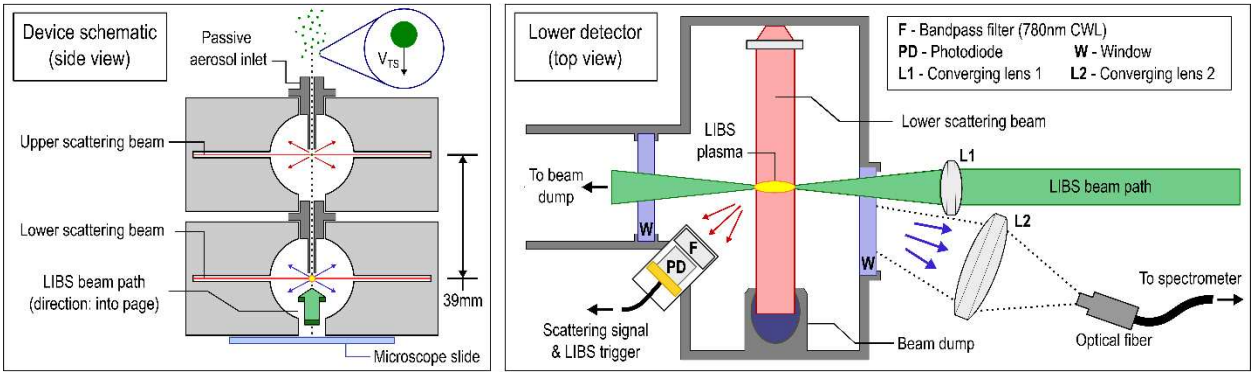

Figure 2.1: A schematic of the DRPS. (Left) Settling particles enter the passive inlet and transit two low-power continuous beams, scattering the incident laser light. A microplasma is formed coincident with the lower scattering beam by a high-power laser pulse. (Right) A top-down view of the lower particle detection region including LIBS system and plasma emission collection optics.

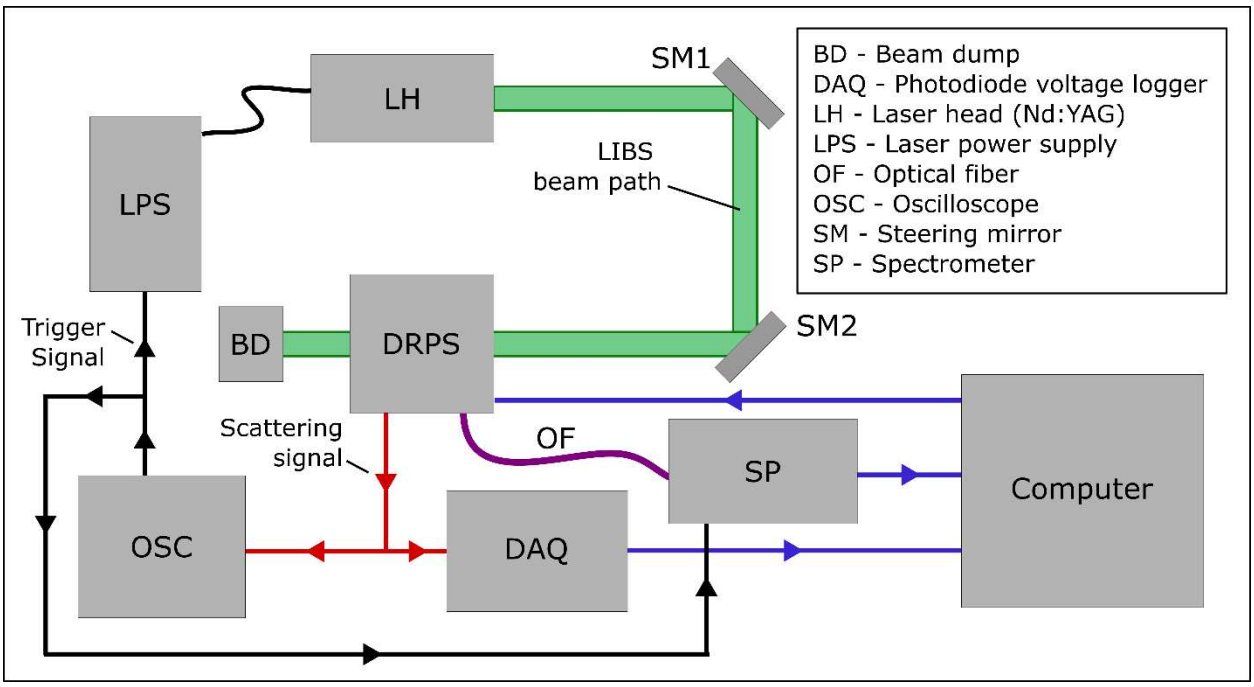

Figure 2.2: An overview of the experiment setup including signal input and output. Communication with the computer is shown in blue, the path of the LIBS and spectrometer trigger signal in black, and light scattering detector signal in red.

2.2 Particle detection & sizing

The method used to size and count particles is based on scattering of laser light as particles pass through the device at their terminal settling velocity. The aerodynamic diameter is determined by measuring the particle time-of-flight between two vertically separated beams (each projecting light orthogonal to and intersecting the settling particle pathline). The current prototype DRPS hardware is based on two commercial particle counters (9301P-OEM, Particles Plus Inc., Stoughton, MA) modified to detect large particles and connected in series. The inlet and outlet of the DRPS are open to ambient air, allowing particles to settle through a small passive inlet (1.5 mm diameter) under the influence of gravity alone. Except for the inlet and outlet, the sampler is fully enclosed to minimize the effect of room air currents that could potentially change the vertical trajectory of the falling particles after entering the device. Each Mie scattering beam is generated using a 785

nm diode laser collimated and focused into a thin sheet with thickness ~50 μm in the direction of the aerosol flow and width ~3 mm in the transverse direction. Light scattered by falling particles as they transit each beam is collected by a photodiode. For the upper beam, the light collection is at a 90º scattering angle, whereas the collection is at 135º for the scattering of the lower beam as not to obstruct the LIBS beam path. An intermediate 1.5 mm diameter inlet separates the regions associated with the upper and lower Mie beams and provides enough optical isolation to prevent cross-talk between the two detector channels. An optical bandpass filter with a 780 nm central wavelength (FL05780-10, Thorlabs Inc. Newton, NJ) is placed in front of each detector to minimize the influence of ambient light. The voltage output from each photodiode is monitored using a USB voltage logger (DI-1120, DATAQ Instruments Inc. Akron, Ohio) sampling at 80 kHz per channel. The minimum detectable particle size can be adjusted by specifying the input current of each laser diode such that only particles of sufficient size scatter enough light to generate a detectable voltage peak. The laser operating current for all testing described in this work has been selected such that particles smaller than ~20um will not produce a scattering signal voltage high enough to trigger a LIBS pulse. The time-of-flight for a given particle is found as the elapsed time between the maxima of the two Mie scattering signals from the upper and lower beams. The particle settling velocity is then found by dividing the known vertical beam separation (3.9 cm) by the time-of-flight. The time-of-flight approach requires that the Mie signals from the two beams be attributed appropriately to the falling particles. For each voltage peak in the record of the lower photodiode, a MATLAB (R2021a, MathWorks Natick, MA) script is used to find a corresponding peak in the upper photodiode record. For the initial validation of the time-of-flight sizing process and testing described in this work, all upper-lower beam scattering signal pairs generated by the script were manually verified and signal logs monitored for potential particle overtake events or

transmission losses. An analysis of coincidence error (i.e., multiple particles transiting the scattering beams simultaneously) and the effect on maximum allowable particle flux through the DRPS is examined in Section 3.3.

2.3 LIBS plasma formation & light collection

The propagation axis of the LIBS beam is oriented horizontally and orthogonal to the Mie scattering beams. The path of the LIBS beam is positioned slightly below the centerline of the lower scattering beam and aligned such that the resulting microplasma (~0.5 mm^3 in volume) is positioned coincident with the path of the falling particles in the horizontal plane. The LIBS beam is generated by an Nd:YAG laser (Ultra, Big Sky Laser Bozeman, MT) with pulsed output (~6 ns) at a wavelength of 1064 nm. The beam has a diameter of 4.5 mm and is focused by a positive lens of focal length 40 mm (LA4130-ML, Thorlabs Inc. Newton, NJ) to a waist of ~50 μm at the location of the aerosol stream. We operate with delivered laser pulse energy of 41+/-2 mJ (based on shot-to-shot variation) which is sufficient to achieve reliable plasma breakdown (~100% of laser shots) in laboratory air regardless of the presence of large particles. The fraction of laser energy not absorbed by the plasma is transmitted to a beam dump to avoid surface ablation and heating inside the DRPS detection volume to mitigate residual air currents. The beam enters and exits the sampler volume through UV-grade fused silica windows (WG41050-C, Thorlabs Inc. Newton, NJ). We estimate the laser plasma to be an ellipsoid approximately 2-3 mm long in the direction of the spark-forming laser and ~200-700 μm in both orthogonal directions. This approximate estimate is based on measurements of plasma kernels reported in the literature [52,64,65]. The focusing optics of the LIBS laser (and LIBS trigger timing) were aligned to maximize the spatiotemporal overlap between the microplasma and the path of the falling particles (as defined by the entry inlet of ~1.5 mm diameter at top of apparatus). Given these dimensions, we estimate

that the plasma covers approximately 45% of the projected area of the falling aerosol stream. If the trajectory of a falling particle does not intersect the microplasma, then it will not be ablated and the resulting spectrum (which is still recorded based on the Mie trigger) will contain only emission peaks from the room air. The dimension of the inlet orifice was chosen to provide a rough balance between LIBS hit rate and measured particle count rates. The orifice opening size presents an area of potential optimization, which is discussed later.

The light emitted from the LIBS microplasma is collected by a 4 cm focal length lens (LA4306-ML, Thorlabs Inc. Newton, NJ) that is positioned at roughly 45 degrees in the back-scatter direction and imaged with 1:2 magnification onto the bare end of a 1.5 mm core diameter optical fiber (M93L, Thorlabs Inc. Newton, NJ) coupled to a USB spectrometer (HR4000, Ocean Insight Orlando, FL). The spectrometer records spectral data over a wavelength range of 250-1100 nm using a 25 μm wide entrance slit and a 3648-pixel charge-coupled device (CCD) detector, resulting in a resolution of ~2.3 nm (peak FWHM). A single spectrum is collected each time the Nd:YAG laser fires using the provided software (OceanView v2.0.8, Ocean Insight Orlando, FL). Post-processing of raw spectra and emission peak detection is performed by a MATLAB script described in Chapter 5.

2.4 Laser timing & triggering

An oscilloscope (TD5034B, Tektronix Inc. Beaverton, OR) is used to generate a signal to trigger the LIBS laser pulse and simultaneously begin spectral acquisition. Specifically, the oscilloscope is used to monitor the voltage output of the lower photodiode and, when a trigger threshold of 0.5 V is reached, a brief 5 V trigger pulse is sent to both the Nd:YAG laser and USB spectrometer. The trigger pulse initiates the 3ms spectrometer integration period and activates the laser's flashlamp. After an additional fixed delay of 226 μsec to allow gain buildup within the laser, the

output pulse is produced. After each laser pulse event, a holdoff period of 500 ms is imposed, during which the LIBS laser does not fire. The holdoff period is to allow any flow disturbances caused by the laser spark shockwave to subside before subsequent probing. The shockwave generated from the plasma formation was found to potentially resuspend particles deposited on surfaces within the DRPS, particularly around the aerosol orifice directly above the lower scattering beam. In the event that these resuspended particles enter the scattering beam, the corresponding signal will cause the LIBS system to fire again unnecessarily. It was determined experimentally that a holdoff period of 500 ms was sufficient to avoid any erroneous LIBS trigger signals due to resuspended particles. An illustrative schematic of the scattering signal time-of-flight measurement and details of the timing and triggering scheme can be found in Figure 2.3.

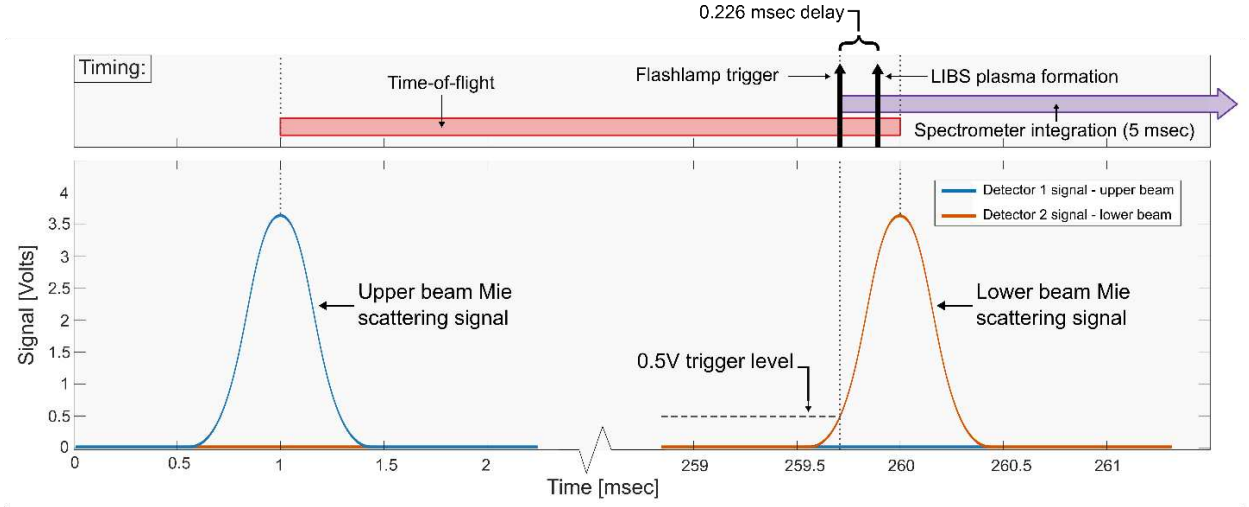

Figure 2.3: Timing diagram with time-of-flight measurement and trigger timing of LIBS laser source and spectral acquisition for an illustrative pair of scattering signals. The peak-to-peak time in this example of 259 msec and vertical beam separation of 39mm results in a settling velocity of 15 cm/sec and corresponds to a particle with an aerodynamic diameter of ~70 µm.

The lower photodiode does detect the light from LIBS plasma; however, this interference is timed to occur *after* a suitable time-of-flight determination has been made. When the LIBS system is active, the light flash from the plasma is detected by the bottom scattering detector. This additional light source potentially interferes with the second (lower) Mie scattering signal. Therefore, the

time-of-flight measurement is computed as the time between the peak of the top detector scattering signal and the voltage peak associated with the LIBS plasma flash in the bottom detector. The time difference between the LIBS plasma voltage spike and the inferred location of the peak of the Mie scattering signal is on the order of 100s of μsec at the most, based on knowledge of the triggering scheme and results with the LIBS system deactivated. The transit time between the two beams ranges from 100s of msec to multiple seconds at the current beam separation of 3.9 cm. Therefore, an error on the order of microseconds results in a negligibly small error (<1% in all cases examined) in the predicted aerodynamic diameter. With the LIBS system active, the direct particle size verification procedure with microscope images (detailed in Section 3.1.1) is not possible due to ablation of particles. To investigate any potential difference in aerodynamic diameter sizing caused by the LIBS system active, a mock analysis was performed using the predicted time at which the LIBS light would have flashed (based on known triggering delay) as the second time marker. The predicted time was calculated as 226 μsec (the delay between the Nd:YAG flashlamp trigger signal and plasma formation) after the instant the scattering signal reaches the trigger threshold value of 500 mV. The particle size statistics obtained with the LIBS system turned off and the simulated LIBS-on timing differ by much less than the particle size detection limits of the system (the difference in median diameter for simulated LIBS-off and LIBS-on conditions was less than 0.1 μm). This calculation reflects only timing considerations associated with the temporal difference between the trigger signal rising edge and true signal peak rather than other effects of the LIBS plasma (flow disruption, electrical interference, etc.), which are addressed by the trigger holdoff period.

2.5 Test aerosol selection & dispersion

Six test aerosols with five distinct compositions and two particle shapes were examined in this work. Four of the six particle types were used to test and validate the time-of-flight sizing system and consist only of microspheres. The microspheres are assumed to be nominally spherical (χ=1) and separated into a series of size bins each spanning a diameter range of ~10-20 µm. Time-of-flight sizing test aerosols cover a range of aerodynamic diameters from 24 to 125 µm and bulk densities from 1025 (polyethylene) to 7800 (stainless steel) kg/m^3. The diameter and circularity of the microspheres was verified using the microscopy procedure described in the next section.

An additional four test aerosol types were used to evaluate the LIBS system and spectral analysis methods. Two of the test particles—fluorescent green polyethylene (PE) and silver-coated soda lime glass (Ag-glass) (UVPMS-BG-1.025 & SLGMS-AG, Cospheric LLC Santa Barbara, CA)—are microspheres and used for both the aerodynamic diameter sizing and LIBS composition validation. The other two test aerosols are polydisperse metal powders with amorphous particle shape covering a continuous and much broader size range than the spherical particles. As reported by the manufacturer, the copper has maximum a size of 75 µm while the titanium has average particle size of 45 µm (207780 & 366994, MilliporeSigma St Louis, MO). For each of the four aerosol materials used in LIBS testing, the locations of the five strongest emission peaks were identified for a total of 20 wavelength values of interest. The target wavelengths for copper and titanium were based on the 5 strongest peaks within the detection range based on the NIST spectral database[41,66]. The five strongest emission peaks were determined experimentally for each of the other two test aerosols, which are comprised of multiple materials in an unknown ratio. Details of the size, shape, and additional relevant properties of all test particles used in this work are compiled in Table 2.1.

Table 2.1: Summary of test aerosol samples used in this work for validation of the particle sizing and composition analysis methods.

Material & Particle type	**Size† [µm]**	**Density† [kg/m^3]**	**Used for particle sizing or LIBS testing?**	**Particles with circularity ≥0.85‡**	**Median da‡ [µm]**	**Emission wavelengths of interest [nm]**
Stainless steel (microspheres)	29-37	7800	Particle sizing only	79%	92	
Titanium (microspheres)	37-47	4540	Particle sizing only	77%	103	
Silver-coated glass (microspheres)	3 size bins: 20-27, 40-48, 63-75	2560-2750	Both	91%	3 size bins: 39, 71, 114	328.1, 338.3, 520.9, 546.6, 589.1
Polyethylene (microspheres)	5 size bins: 27-34, 38-45, 53-63, 75-90, 106-125	1025	Both	80%	5 size bins: 35, 44, 60, 81, 126	386.0, 415.4, 514.8, 589.1, 656.3
Copper (Polydisperse metal powder)	45 (average)	8960	LIBS only		13	324.8, 510.6, 515.3, 521.9, 578.0
Titanium (Polydisperse metal powder)	75 (maximum)	4540	LIBS only		19	308.8, 323.6, 334.9, 376.0, 430.0

† Size, composition, and density data provided by the manufacturer.

‡ Circularity and aerodynamic diameter measured via microscopy.

Due to the large size of the test aerosols and the need for low particle concentration, common dispersion methods such as a nebulizer or fluidized bed generator were not appropriate. Instead, test particles were dispersed in the laboratory by generating a small jet of air with a rubber squeeze bulb to eject a small quantity (<1 mg) of material through a copper pipe into the air above the

DRPS. The outlet of the copper pipe is oriented vertically and positioned ~70 cm above the sampler inlet. The largest particles used in this work have d_a ~ 125 µm and would reach their terminal settling velocity (36 cm/s) after falling a distance of only 3.5 cm. Smaller particles will reach V_{TS} over an even shorter distance. Thus, all test aerosols are given sufficient vertical distance to reach their terminal settling velocity before reaching the DRPS inlet. The air volume in which the aerosols are dispersed is constrained by a 20 cm diameter 120 cm tall open-ended tube, which contains the particle cloud and reduces the influence of room air currents. A diagram of the test aerosol dispersion method used for all experimentation described in this work is presented in Figure 2.4.

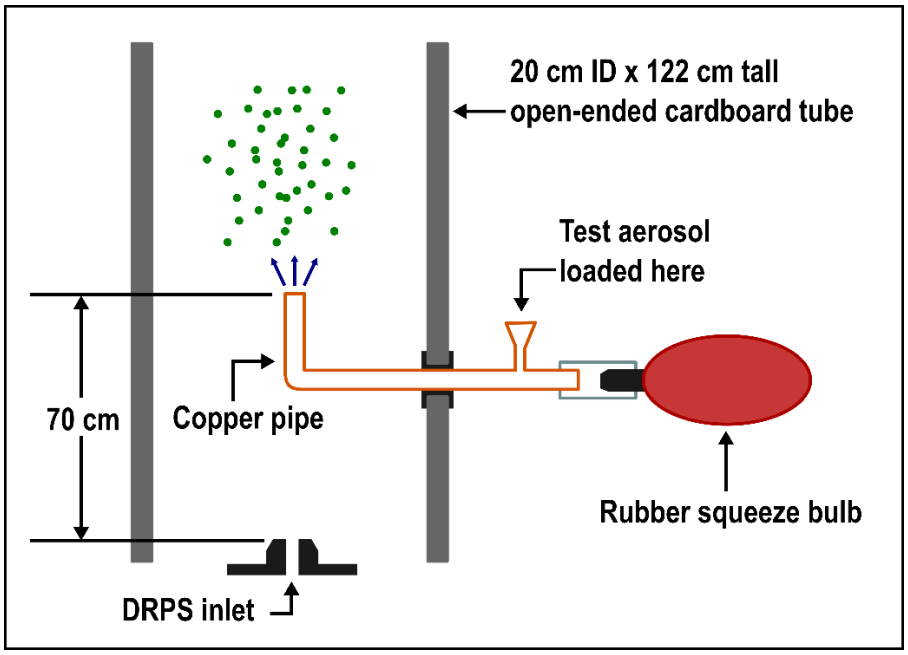

Figure 2.4: A diagram of the test aerosol dispersion mechanism. The rubber squeeze bulb creates a blast of air, propelling a small volume of test aerosol into a large cardboard tube above the DRPS inlet.

2.6 Particle microscopy

The particle size ranges as specified by the manufacturers are provided in Table 2.1 for all test aerosol types used in this work. The size distributions were also verified using microscope images.

Test particles were dispersed onto glass microsphere slides using the procedure detailed in the previous section and images were captured using a microscope (Orthoplan, Leitz Wetzlar, Germany) and USB camera (GRYPHAX, Jenoptik AG, Germany). The quantity dispersed on each slide was controlled to avoid touching or overlap of particles in the images. Therefore, agglomerated groups of aerosols were rarely encountered during this procedure and were manually excluded from the sizing measurement when present to obtain sizing information from only single particles. At the magnification value used (6.3x), a single pixel in the captured images corresponds to a 1.2 µm x 1.2 µm square. Therefore, the measured diameters are reported to the nearest micrometer and very small sub-micron particles are not captured in the images.

To measure the actual size distribution of the test aerosols, microscope images were processed using ImageJ image analysis software [67] to convert the grayscale images to black and white only, where black regions represent the particles (Figure 2.5). After image processing, the projected area of each particle was measured and converted to an area equivalent spherical diameter. Assuming the particles are spheres, the spherical equivalent diameter (d_{eq}) is computed using Eqn. (2.1), where A_{proj} is the projected area (in μm^2) of an individual particle in the microscope images.

$$d_{eq} = 2\sqrt{\frac{A_{proj}}{\pi}} \tag{2.1}$$

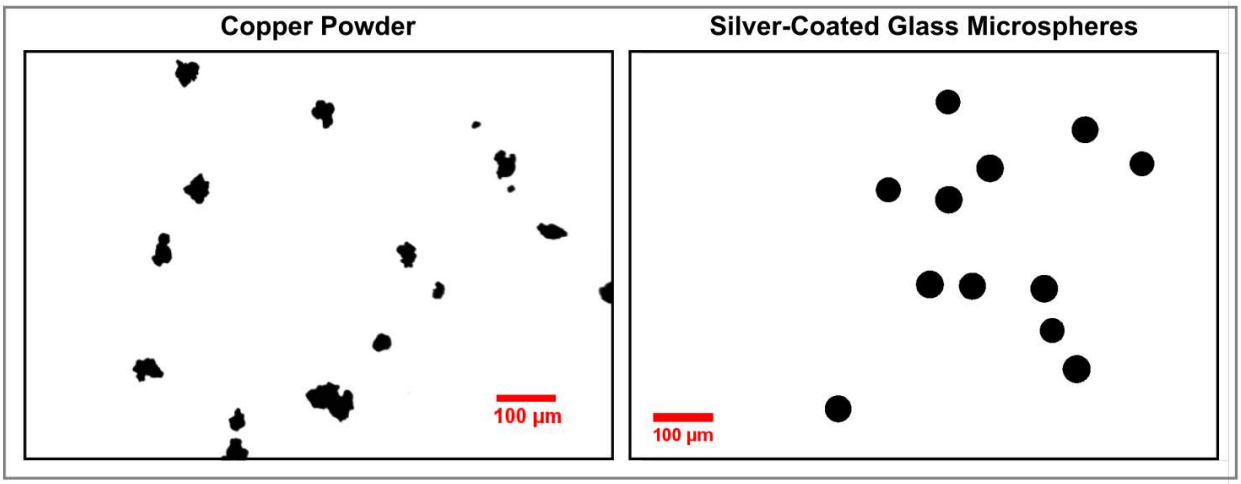

Figure 2.5: Representative microscope images of two test aerosol samples: copper powder (Left) and silver-coated glass microspheres (Right).

Histograms of the area equivalent diameter measurements for all test aerosol types are presented in Figure 2.6. The two microsphere samples consisting of multiple size bins (PE and Ag-glass) were dispersed and measured as a mixture of all bins at this stage. Additionally, a representative sample of each microsphere material and size bin was examined for circularity. Circularity is computed by ImageJ software using Eqn. (2.2):

$$Circularity = 4\pi\left(\frac{A}{P^2}\right) \tag{2.2}$$

where A is the projected area of an individual particle and P is its perimeter. Figure 2.7 below contains a histogram of the circularity of all stainless-steel microspheres examined with an inset example of a single microscope image including circularity labels for each particle. The majority (79.4%) of particles are round, defined as those with circularity ≥ 0.85.

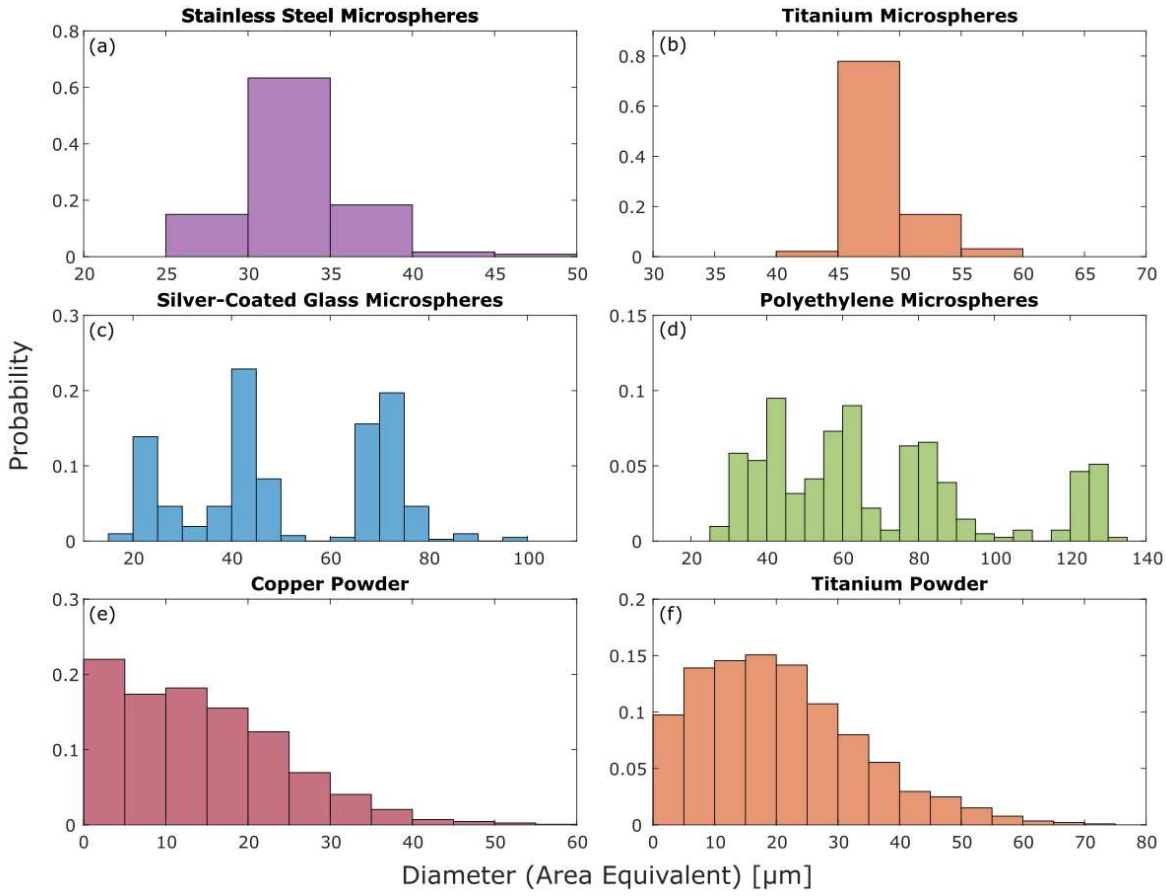

Figure 2.6: Particle size distributions of area equivalent diameter (d_{eq}) measured from microscope images for all test aerosol samples: (a) stainless steel microspheres, (b) titanium microspheres, (c) silver-coated glass microspheres, (d) polyethylene microspheres, (e) copper powder, and (f) titanium powder. Histogram bin widths for each plot are 5 µm.

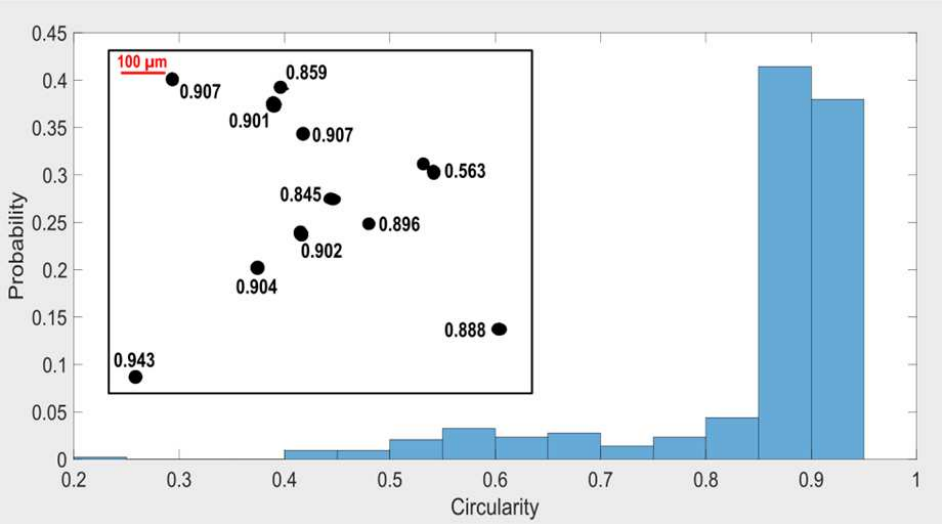

Figure 2.7: Histogram of circularity computed with Eqn. (2.2) for stainless steel microspheres and a representative image containing the circularity value for each measured particle.

CHAPTER 3 – AERODYNAMIC DIAMETER MEASUREMENT

3.1 Methods

3.1.1 Particle size verification

Microscopy was used to verify the count and size of particles passing through the DRPS inlet. The accuracy of the aerodynamic diameters determined by DRPS time-of-flight was evaluated against microscope images of the same test aerosols, along with knowledge of particle density. A glass microscope slide was held in a fixture under the sampler such that the same particles measured by the scattering beams were deposited onto the slide. The test aerosols used to validate the time-of-flight particle sizing method were all microspheres rather than amorphous "real" aerosol shapes to reduce errors associated with estimating the dynamic shape factor when converting from d_{eq} to d_a. Most of the particles examined in the microscope image size verification procedure were nominally round; however, some non-spherical particles were present. Non-spherical particles are attributed to either manufacturing anomalies or doublets/agglomerates of spherical particles. The frequency of non-spherical particles varies slightly with material and particle size. Based on the circularity analysis described in Section 3.2, the majority (>75%) of particles could be considered spherical for every microsphere size bin and material. Therefore, it is reasonable to assume a large majority of microsphere particles have $\chi \sim 1$.

The equivalent diameter measurements obtained from the microscope images are converted to aerodynamic diameter using the particle density specified by the manufacturer and Eqn. (1.2) for direct comparison with the sizing results of the time-of-flight method. Plots of the cumulative distribution function (CDF) were generated to visualize and quantify the agreement between the

number size distributions found from time-of-flight (d_a) and those from microscopy (d_{eq}) for each test particle material and size. A two-sample Kolmogorov-Smirnov (KS) test was used to test for a statistically significant difference between the empirical CDFs for each sizing method. In addition to the result of the KS test, the total particle counts obtained by each method, the median, 1st and 3rd quartile values were computed for comparison.

3.1.2 Counting efficiency

The counting efficiency (η_{count}) represents the fraction of all particles entering the device which are successfully counted and sized. The number of entering particles is found as the number of scattering events in the top beam while the number of particles counted and sized is found as the number of particles yielding a pair of scattering signals that can be paired to compute a transit time:

$$\eta_{count} = \frac{\#\ of\ time{-}of{-}flight\ signal\ pairs}{\#\ of\ particles\ entering\ instrument} \tag{3.1}$$

Factors that reduce the experimental counting efficiency include transmission losses between the two scattering beams and coincidence error. Particle losses occur due to the trajectory of falling particles deviating from the vertical direction, thereby causing them to deposit on surfaces (e.g. intermediate inlet) between the upper and lower beams. Coincidence error is defined in the context of this work as cases where the scattering signal appearance rate in the bottom beam exceeds the inverse of the transit time of the smallest particles of interest. If the flux of particles into the device exceeds the coincidence error limit, it cannot be ensured that no more than a single particle exists between the scattering beams at one time. If multiple particles are settling between the scattering beams simultaneously, it remains possible to pair the upper end lower beam scattering signals. However, the signal pairing process becomes more complicated and must be performed manually

(or manually verified). The counting efficiency is reduced whenever an upper beam scattering signal is unable to be paired to a corresponding lower beam signal—whether due to transmission loss, coincidence error, or any other reason.

3.2 Time-of-flight sizing results

Aerodynamic diameter measurements made by the DRPS and by optical microscopy are presented in Table 3.1 for each material type and particle size range (as specified by the manufacturer). Summary statistics appearing in Table 3.1 for each test aerosol were computed from a combined dataset of multiple experimental trials (3-8 trials depending on size and material). The measured aerodynamic diameter distributions inferred from the DRPS time-of-flight agree closely with those found by microscope imaging over all particle sizes and compositions. The greatest deviations occurred at the upper tail of the "33-44μm" Ag-Glass spheres and the lower tail of the "81-103μm" stainless steel particles. However, across both of these distributions the median, 25^{th}, and 75^{th} diameter sizes differed only between 1-4 μm (see Table 3.1 and Figure 3.2). Results from the 2-sample KS tests suggest that the DRPS and optical microscopy methods reported similar underlying size distributions across all test aerosols (Table 3.1; no rejection of the null hypothesis that distributions are similar at the 95% confidence level for any test aerosol type).

Agreement between median diameters reported by the two methods was excellent, as shown in Table 3.1 and Figure 3.1. A Deming regression of median sizes measured across the full range of tested diameters gave a slope of 0.988, an intercept of 0.02 μm and an r^2 value above 0.999. This regression matches the 1:1 line shown in Figure 3.1 well. The mean absolute difference between the median aerodynamic diameters measured by the instrument by time-of-flight and microscopy over all 8 test aerosol types was 0.9 μm with a mean difference in interquartile range of 1.9 μm;

these values are close to the uncertainty limits of the optical microscopy procedure itself, which are on the order of 1 μm for the imaging/magnification system used here.

Table 3.1: Comparison of measured size distributions from particle time-of-flight and optical microscopy.

d_a [μm]† Material	**Trials**	**Sizing Method**	**Total Counts [n]‡**	**Median [μm]**	**25th,75th percentile (IQR) [μm]**	**2-sample KS test p-value**
33-44μm Ag-glass	4	Microscope	85	39	36, 42 (6)	p=0.27
		Time-of-Flight	83	40	36, 46 (10)	
66-80μm Ag-glass	2	Microscope	89	71	68, 73 (5)	p=0.85
		Time-of-Flight	90	71	67, 73 (6)	
100-120μm Ag-glass	4	Microscope	90	114	110, 118 (8)	p=0.55
		Time-of-Flight	94	115	110, 119 (9)	
27-34μm Polyethylene	5	Microscope	48	35	32, 37 (5)	p=0.8
		Time-of-Flight	52	34	32, 36 (4)	
54-64μm Polyethylene	8	Microscope	88	60	55, 63 (8)	p=0.98
		Time-of-Flight	88	60	56, 63 (7)	
107-127μm Polyethylene	5	Microscope	52	126	122, 128 (6)	p=0.065
		Time-of-Flight	52	124	122, 127 (5)	
78-100μm Titanium	6	Microscope	95	103	101, 106 (5)	p=0.19
		Time-of-Flight	94	104	101, 107 (6)	
81-103μm Stainless Steel	5	Microscope	119	92	88, 96 (8)	p=0.23
		Time-of-Flight	120	92	84, 97 (13)	

† Size, composition, and density data provided by the manufacturer.

‡ Total counts represent a summation across all trials.

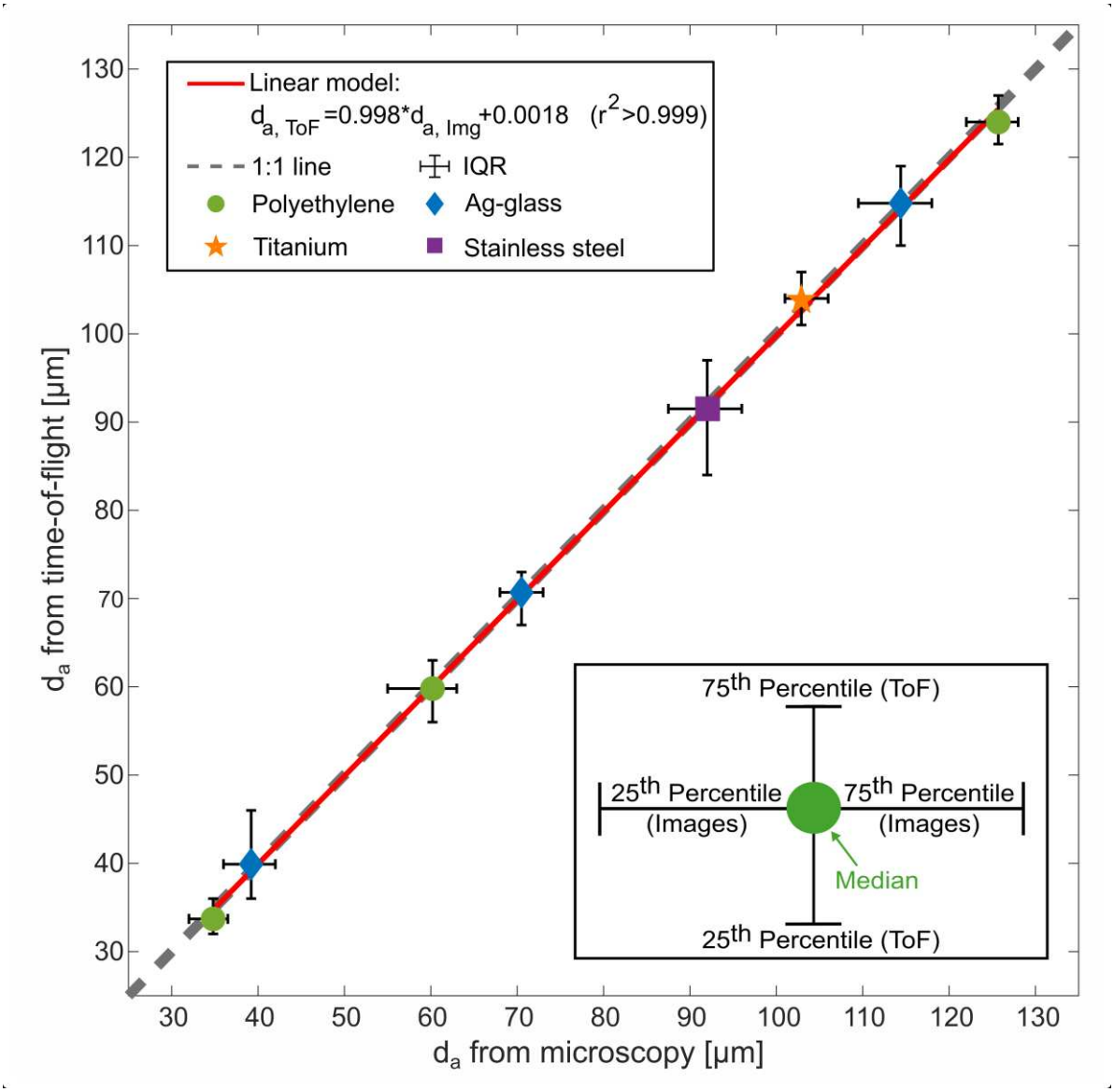

Figure 3.1: Linear regression of median aerodynamic diameter measurements obtained by time-of-flight and microscopy. Vertical and horizontal bars indicate the interquartile range of aerodynamic diameter measurements for each method (time-of-flight and microscopy, respectively).

An additional comparison of the size distributions measured by the time-of-flight method and microscopy is provided in the form of box plots (Figure 3.2). Boxes with green borders represent the equivalent diameter sizing results from the microscope images and blue borders for the time-of-flight aerodynamic diameter measurements. The extent of the boxes shows the interquartile

range (IQR) with whiskers extending to the most extreme data point not considered an outlier. Red "+" markers indicate outliers, defined as data points greater than 1.5 times the IQR away from the top or bottom of the box. The notches on either side of each box represent a 95% confidence interval on the median value (red line). The gray shaded regions indicate the aerodynamic diameter range specified by the manufacturer for each test aerosol.

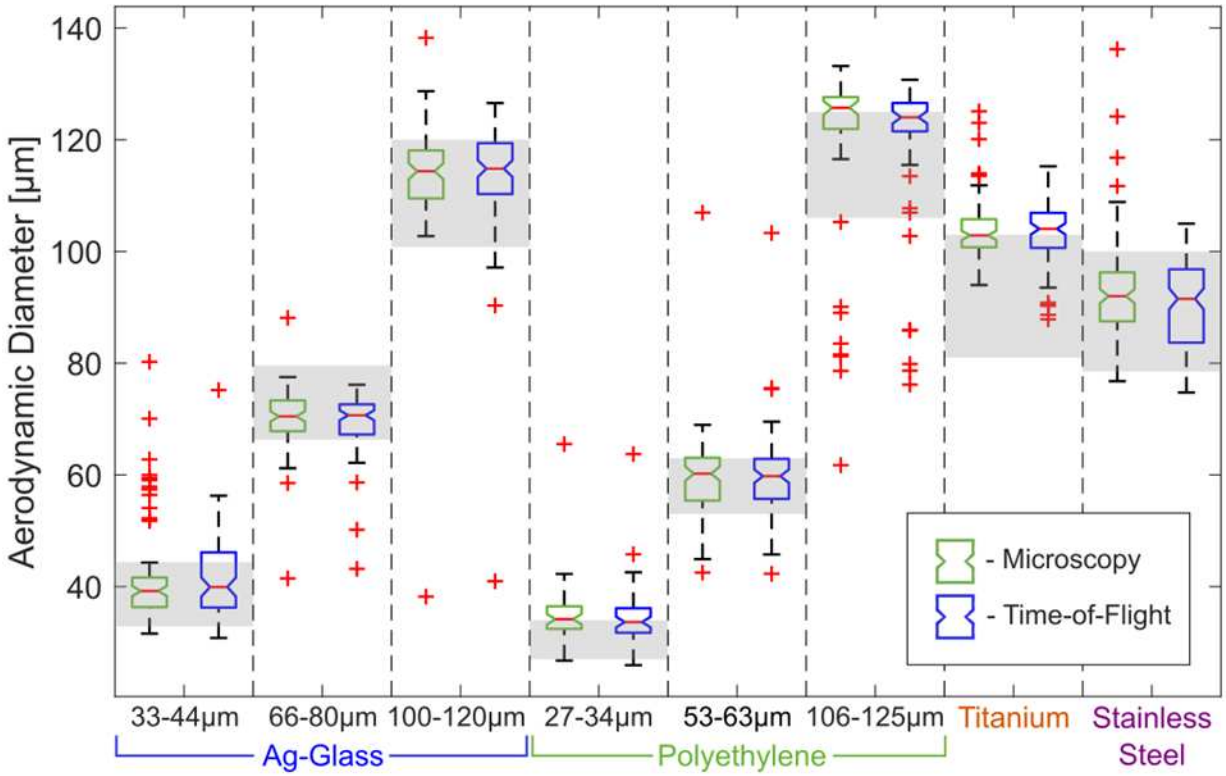

Figure 3.2: Boxplots of aerodynamic diameter distributions measured by time-of-flight and microscopy for all microsphere samples. The gray shaded regions correspond to the aerodynamic diameter size ranges computed by Eqn. (1.2) using the aerosol size and density information reported by the manufacturer.

The number of usable scattering signal pairs for time-of-flight measurements and the number of particles captured in the microscope images were similar, which indicates that most particles detected and sized by the DRPS eventually deposited on the glass slide and were captured in the microscopy step. The particle count on the microscope slide and the number of particles detected

by the instrument were equal in 21 of 38 trials. For the 17 trails where the total counts differed, the discrepancy in microscope slide versus time-of-flight particle counts was ≤10% in all but 2 trials (and never greater than 3 counts). Low slide counts can be attributed to losses as particles may deposit inside the sampler or otherwise fail to reach the microscope slide and/or unusable Mie scattering signals (below the voltage threshold or rejected due to coincidence error). Particles may also be miscounted if they settle on top of each other and agglomerate (though this artifact appears infrequent based on collected microscope images). When non-spherical particles are encountered in the images, the equivalent spherical diameter skews larger than the true aerodynamic diameter. For initial device validation, work has focused on spherical particles over relatively narrow size ranges. Opportunities for hardware optimization to facilitate operation with polydisperse samples are discussed in the Efficiency & Optimization section.

3.3 Efficiency & optimization

Potential instrument performance limitations in the field (and to motivate possible future modifications) were investigated by modeling hypothetical particle counts for several assumed particle size distributions and mass concentrations. The instrument is configured to detect all particles larger than some minimum particle diameter D_1 (set by the detector voltage threshold) which we take here as 20 µm. The instrument count rate φ (number of counts per unit time) is then found as the flux of particles through the inlet integrated over a specified size distribution:

$$\varphi = \int_{D_1}^{D_2} \frac{dN}{dD} A_i V_{TS}(D) dD \tag{3.2}$$

where A_i is the area of the inlet, dN/dD is the specified particle number distribution function, and D_2 is the largest particle to be detected. (The D_2 limit can be set as infinity given that even the largest particles of interest readily fall through the inlet in practical designs). A practical

consideration is that, to avoid coincidence error (i.e. the presence of multiple particles between the Mie beams at a given instant which may confound the pairing algorithm), one should set an upper limit on the final count rate φ. Specifically, the smallest particles of interest, with d_a = 20 µm, require 3.3 seconds to settle through the two beams (for current separation of 39 mm), meaning that the instrument count rate should be limited to a maximum of 0.3 particles/sec. For illustrative exposition of instrument performance, a lognormal particle size distribution with a geometric mean diameter 30 µm and a geometric standard deviation of 1.5 was assumed in the following calculations. With the current design, the DRPS could operate reliably at ambient aerosol mass concentrations up to 144 µg/m^3 before the coincidence error limit. The maximum mass concentration (before the coincidence error limit) is inversely proportional to the beam separation, e.g., if the beam separation were reduced by a factor of 3 (to 1.3 cm) then the maximum allowable mass concentration increases to ~430 µg/m^3. Furthermore, reducing inlet diameter reduces the particle flux in proportion to its area (diameter squared). Increasing the inlet area admits more particles to the device but increasing beyond the dimension of the Mie beam or LIBS plasma will not generally be useful. These parameters can be optimized to yield needed instrument performance in different environments (i.e. for different particle distributions). A practical consideration is that reducing inlet orifice sizes will also tend to increase the probability of particles depositing within the inlet tube.

Studies of occupational exposure to inhalable aerosols of welders have measured mass concentrations in the range of 0.53 – 11.6 mg/m^3 depending on the type of welding with a median concentration of 2.48 mg/m^3 [68,69]. The particle distribution produced by automatic welding was found to be bimodal with an approximately lognormal distribution in the coarse mode ($d_a \geq 3.5$ µm) containing 47.9% of the total mass. The coarse mode distribution had a mass mean

aerodynamic diameter (MMAD) of 9.93 µm and GSD of 1.73 [69]. Assuming the current configuration of the DRPS (1.5 mm inlet, 39mm beam separation, and 20 µm minimum detectable particle size) and the mean mass concentration for automatic welding (0.66 mg/m^3), the flux of particles into the device is estimated to be 0.131 particles/sec, or a particle every 7.6 seconds which is reasonable for practical field use. The maximum mass concentration (11.6 mg/m^3) was measured for flux-cored arc welding [68]. Using the same lognormal distribution parameters as the previous case with this mass concentration, the particle flux increases to 2.3 particles/sec. This count rate would exceed the criterion for avoiding coincidence error based on the current design, but the instrument could be modified accordingly. By reducing the inlet area by a factor of ~3 (which would reduce the particle ingestion by ~3 to ~0.8 s^{-1}) and reducing the Mie beam separation by a factor of ~3 (which would increase the maximum allowed count rate by ~3 to ~0.9 s^{-1}), the coincidence error limit would not be exceeded.

Additional results of the particle flux calculation are plotted in Figure 3.3 for 0.5 to 3 mm inlet diameter and 0.5 to 3.9 cm scattering beam separation. Each case assumes the same lognormal size distribution with a count median diameter 30 µm, a geometric standard deviation of 1.5, and a minimum detectable particle size of 20 µm. The maximum mass concentration is calculated for each case for a solution to the particle flux equation (Eqn. (3.2)) that does not exceed the allowable particle flux. For the variable inlet size case, where the beam separation is fixed at 3.9 cm, the maximum flux is 0.3 particles/sec. With variable beam separation, the inlet size is specified at 1.5 mm, and the maximum allowable particle flux is set so that only one particle can exist between the beams simultaneously. The vertical dashed lines indicate the current values of inlet diameter (1.5 mm) and beam separation (3.9 mm).

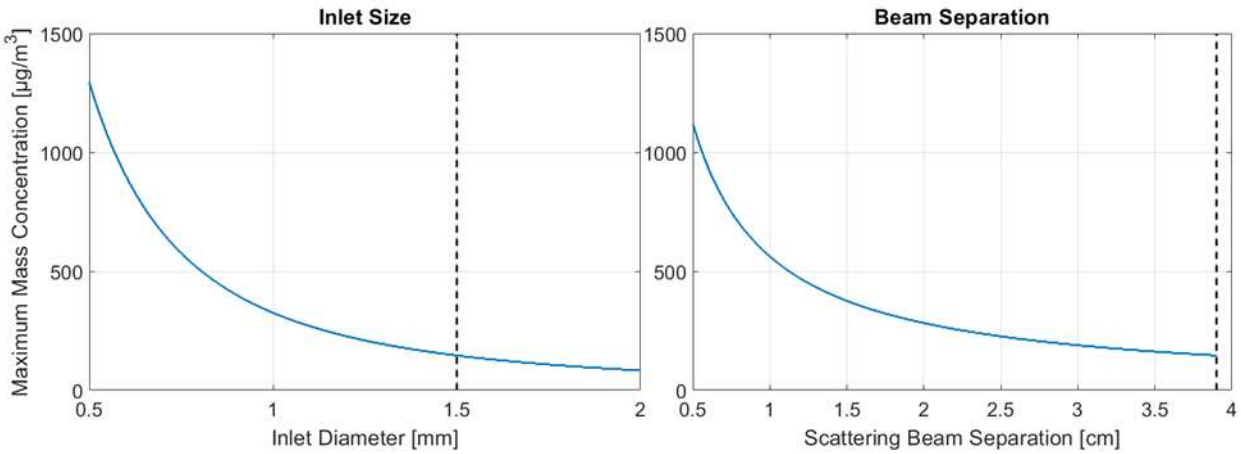

Figure 3.3: Plots of the maximum allowable ambient mass concentration to avoid coincidence error vs the diameter of the DRPS inlet (left) and vertical separation of the Mie scattering beams (right). The dashed lines indicate the inlet diameter and beam separation of the current prototype configuration.

Additionally, we note that room air currents could impact the performance of the current DRPS prototype, as particles will not settle vertically when local air velocities are high. This potential bias will be the subject of ongoing work. We anticipate this bias being minimal based on results from Baldwin and Maynard (1998) who surveyed wind currents across various occupational settings and reported that >85% of measurements were less than 0.1 m/s [70].

Following the validation of the time-of-flight sizing system and prior to the development of the signal classification algorithm, initial LIBS emission spectra were obtained using the prototype device to identify both solid Titanium microspheres and the ~75-225 nm thick silver coating of the Ag-glass microspheres. Example spectra for these materials are provided in Figure 3.4. Examples for both the silver-glass ($d_a \approx$ 66-80 µm) and titanium ($d_a \approx$ 78-100 µm) microspheres are shown compared to the background air spectra. The specific neutral silver (Ag I) lines from the NIST emission database are labeled (328.1, 338.3, 520.9 and 546.6 nm). Peaks associated with the soda lime glass core of the particle are typically not detectable in the experimental spectra due to partial ablation of the particle, though Na I (589.1 nm) Ca I (422.7 nm) and Ca II (393.4 nm) emission

can be seen in the example plot. Titanium emits at a larger number of wavelengths and only the most prominent Ti II peaks are labeled in the figure. The proof-of-concept spectra presented here supported the ability to identify particle species and demonstrated the need for a procedure to eliminate or suppress the background spectral contribution from air breakdown and continuum emission.

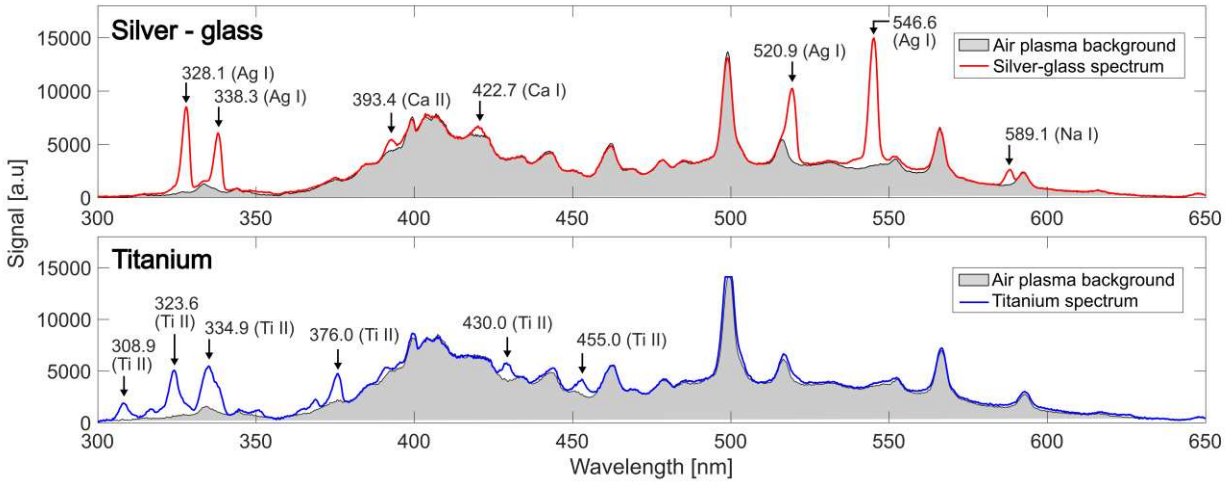

Figure 3.4: Example LIBS spectra obtained from silver-coated glass (top) and titanium (bottom) test aerosols. Shaded regions indicate spectral features associated with breakdown of ambient air. Peaks resulting from ablation of the analyte species are called out with arrows.

CHAPTER 4 – LIBS SPECTRAL ANALYSIS & MATERIAL CLASSIFICATION

4.1 Methods

4.1.1 Experimental signal dataset

Four test aerosols of dissimilar composition were used for LIBS peak detection and automatic classification algorithm validation. The four material classes (silver-glass, polyethylene, titanium, and copper) were dispersed individually. Therefore, only a single test material was assumed to be present in the sampling environment at a given time. However, there is a remote possibility of residual particles from previous trials deposited within the dispersion hardware being resuspended and sampled. The two material types consisting of microspheres (Ag-glass and PE) were initially separated into discrete size bins to facilitate validation of the time-of-flight sizing methods, though a mixture of all size bins for a single material were dispersed simultaneously during LIBS testing. The resulting size distributions obtained by mixing of size bins for each microsphere material appear in Figures 2.6(b) and 2.6(c).

A total of 1380 experimental spectra with approximately equal sample size over the four material classes was recorded. The spectrometer was configured to acquire a signal each time a LIBS pulse was generated, and the energy of each pulse is greater than the breakdown threshold of the laboratory air. Therefore, a single emission spectrum is recorded every time a particle is detected by the lower scattering beam (provided the particle is not detected during the LIBS holdoff period). Because the volume of the microplasma covers only a fraction of the region in which a particle can exist at the instant of the trigger event, each collected signal may or may not contain spectral information from the detected particle. There are, therefore, two possibilities for each LIBS signal:

a particle “hit” in which the particle of interest is ablated by the plasma resulting in detectable emission lines or a particle “miss” containing spectral emission from air only (and continuum emission). A case in which the particle is only minimally ablated by the plasma and no emission lines from the particle species are detectable above the baseline noise level is also possible but can be treated the same as a “miss”. The set of 1380 test spectra contains a mix of signals corresponding to particle hits as well as misses. Additionally, 100 spectra were collected in the absence of test aerosols as a set of known air-only spectra and appended to the initial signals for a final set of 1480 test spectra.

All test spectra were manually and assigned into one of five groups (four test materials and air-only signals) by a human classifier to validate the classifications (of the same signals) made by the spectral analysis algorithm. In general, the testing procedure made clear which particle type was in use and, thus, the expected material present in the signal. Manual classification was required to differentiate between the air-only spectra resulting from a missed particle, cases where emission lines from the expected material are indeed present, and rare cases of residual particles from past tests (i.e., detectable emission from an unexpected material). A plot of each LIBS signal with markers at 20 potential emission peak locations (the five wavelengths of interest for each particle type) was generated for manual classification (see Figure 4.1). The signal was assigned into the corresponding class if the human classifier observed clear emission peaks at multiple wavelength markers for a particular particle type. If no strong emission were found, the signal was assumed to be an air-only spectrum resulting from a missed particle. The human classifier determined 42% of the total spectra to be air-only, consistent with the LIBS hit rate figures achieved in previous testing with these test aerosols. The groups assigned by the manual classification procedure are considered reliable and accepted as the true class for measuring the accuracy of the classification algorithm.

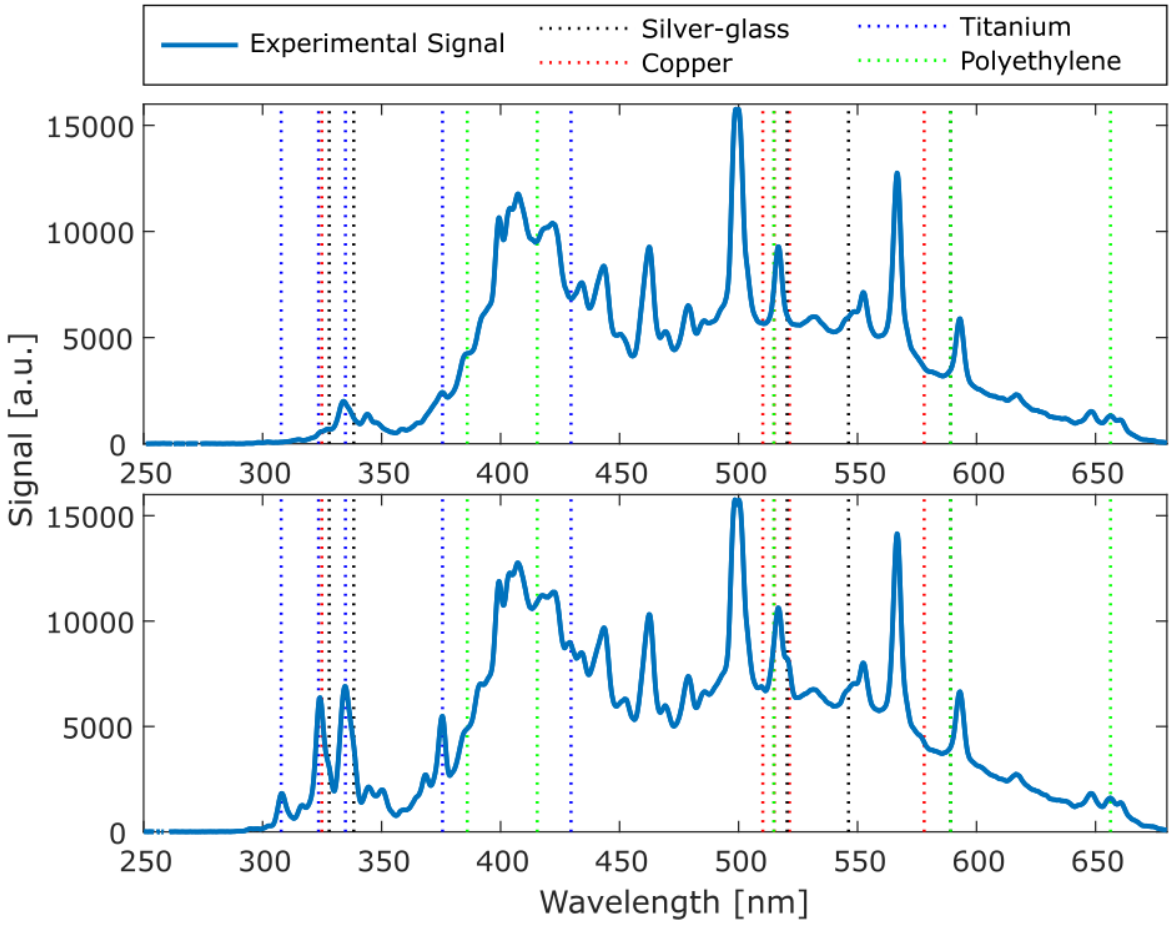

Figure 4.1: Example LIBS signals used in manual classification. Vertical dotted lines correspond to potential emission peak locations for each test material. The signal in the top panel was determined to be an air-only spectrum and the signal in the lower panel was classified as a titanium spectrum.

4.1.2 Data processing & spectral analysis

One of the main goals of the current work is to develop a classification algorithm to determine the elemental composition of the analyte (falling particle), including the possibility of identifying air-only spectra for cases where the laser plasma misses the particle, based on examination of individual test spectra. Here, we evaluate the algorithm's efficacy by comparing the predicted test aerosol class for a given test spectrum versus "truth" values determined from the offline manual classification of the same spectra. The classification algorithm (as applied to a test spectrum)

follows a series of steps, the first of which is a background subtraction to remove contributions from the continuum and air emission lines. This is followed by a second step which uses a threshold approach to look for the presence of analyte lines in targeted regions. Material Scores based on the number of lines detected in the wavelength regions of interest are assigned and used to sort the test spectra into classes corresponding the analyte material composition.

Because the laser beam is incident on particles within ambient air, even in cases where the laser hits the particles, there will inevitably be microplasma formation in air surrounding the particle. The resulting plasmas will therefore always include spectral contributions from air species, such as dissociated and ionized nitrogen and oxygen, which can potentially overlap and interfere with emission lines of the particle species. A scaling and subtraction step was conducted based on an air reference spectrum to mitigate the effect of emission from the air matrix on the particle spectra. The air reference is derived from 100 air plasma spectra recorded at the regular LIBS operating conditions but with no large particles present. While the possibility of small ambient aerosols in the plasma region remains, these particles would also contribute to the air background signal under normal testing. Therefore, the collection of reference air spectra would be repeated if there are any substantial environmental changes such as moving to a new sampling location. The 100 spectra are nominally similar but have some inconsistency in spectral intensity resulting from small shot-to-shot variations in LIBS laser energy and the stochastic nature of plasma breakdown. From these spectra, we determine a final mean air reference spectrum and standard-deviation air spectrum (Figure 4.2). The air reference spectrum is used to suppress spectral contributions from air and continuum emission and the standard deviation spectrum is used for peak intensity thresholding. For each test spectrum, we first find a multiplicative constant scaling factor for the amplitude of the mean air spectrum that brings the test and air spectra to best possible least-squares agreement.

Spectral regions in which strong emission lines from the test particles are anticipated are excluded from the least-squares calculation to obtain a scaling factor that provides the best agreement in regions where only air and continuum emission will be present. The excluded wavelength ranges are identified in Figure 4.2 by gray shaded zones. Regions with spectral intensity ~0 and near the strong, often saturated N II peak at 500.1 nm are also excluded. Examples of a raw test spectrum, scaled air spectrum, and the final post-subtraction spectrum are shown in Figure 4.2. The spectral features associated with continuum emission and air species are suppressed, while the final spectrum exhibits strong emission features resulting from the ablated particle species, which was silver-coated glass in the example presented in the figure.

After the air subtraction, the algorithm looks for the presence of analyte lines from candidate species. Although air features may overlap with the lines of interest, the air plasma subtraction procedure typically eliminates this problem (see 520.4 nm Ag I line with interference from the N II line at 518 nm in Figure 4.2). At each candidate line location, a series of nine data points centered on the wavelength of interest is extracted from the LIBS spectrum to create a detection window ~2 nm wide. If a sufficiently strong peak exists within this window, a single positive peak identification for the corresponding material is recorded. A challenge for spectral line identification is that, owing to variations in plasma formation and in spatial overlap of particle and plasma, the air subtraction step can lead to small anomalous peaks associated with artifacts of the subtraction, i.e., not due to real spectral features, in the final spectrum. One of the functions of peak thresholding in the classifier algorithm is to avoid erroneous detection due to these residual noise features. The condition for positive line detection is based on the peak

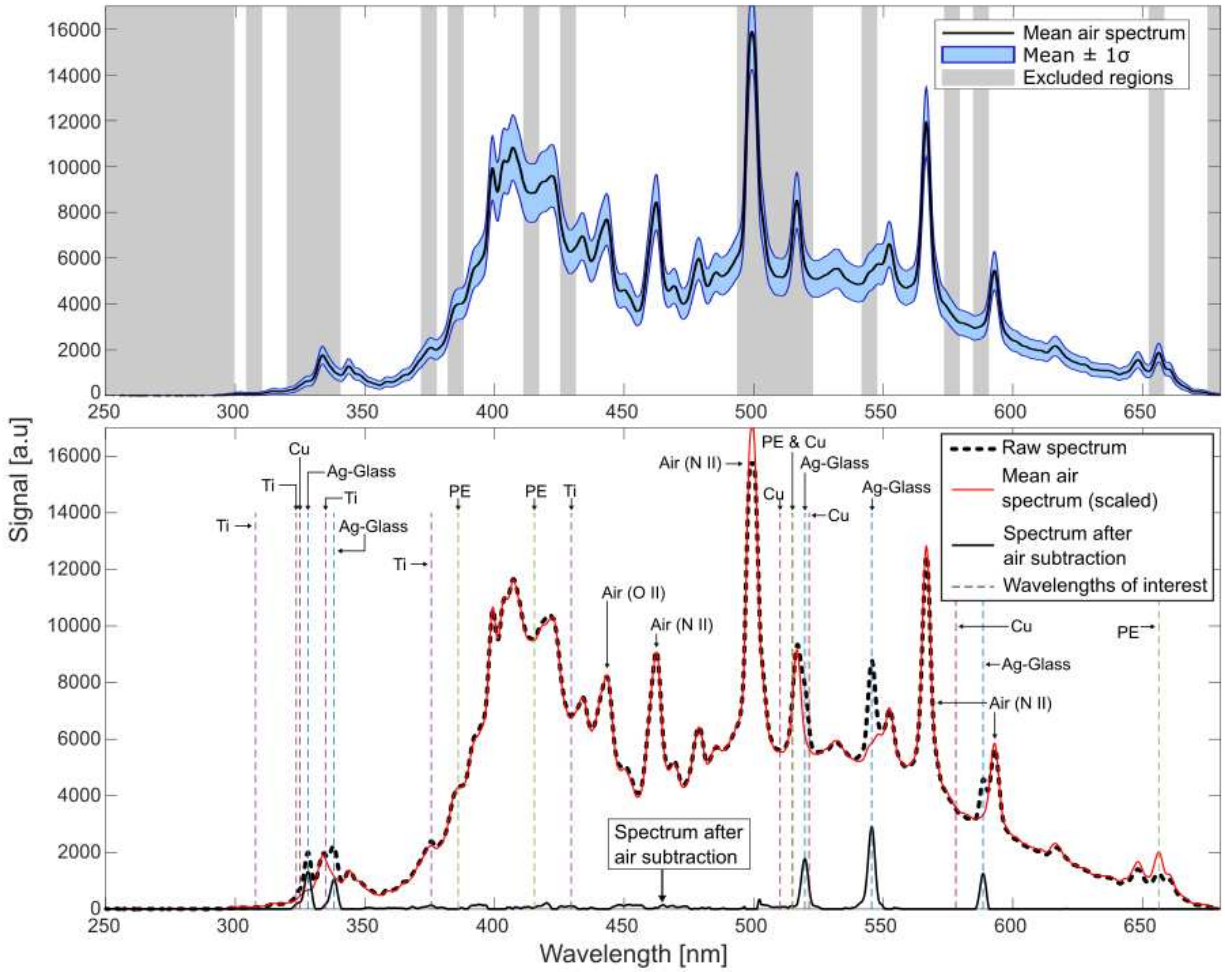

Figure 4.2: (Top) Mean and standard deviation of 100 known air spectra collected in the absence of test aerosol. The gray shaded regions indicate wavelength ranges excluded from mean air scaling factor computation. (Bottom) Example of a raw experimental LIBS spectrum containing emission from air and a silver-coated glass particle, the air spectrum scaled to match this signal, and resulting signal after subtraction of the air spectrum. Wavelengths of interest for all four test materials are denoted by vertical dashed lines.

spectral intensity of the post-subtraction spectrum exceeding a pre-determined value, which we refer to as the Absolute Intensity Threshold (AIT). The AIT depends on wavelength and is determined based on a multiple of the standard-deviation air reference spectrum (e.g., an AIT=0.5σ, where σ is the standard-deviation air reference spectrum, implies a peak intensity must exceed 0.5 times the value of the standard-deviation spectrum at the corresponding wavelength to satisfy the threshold).

An additional prominence threshold (PT) is also applied to each peak to ensure that the intensity of the peak is sufficiently high, relative to the neighboring values. The prominence of a peak is found by extending a horizontal line from the peak in both directions until it crosses the signal again or reaches the edge. The higher value of the two local minima found in the two resulting regions (left and right of the peak) defines the reference level. The peak's prominence is then the vertical distance between the peak value and the reference level (see Figure 4.3).

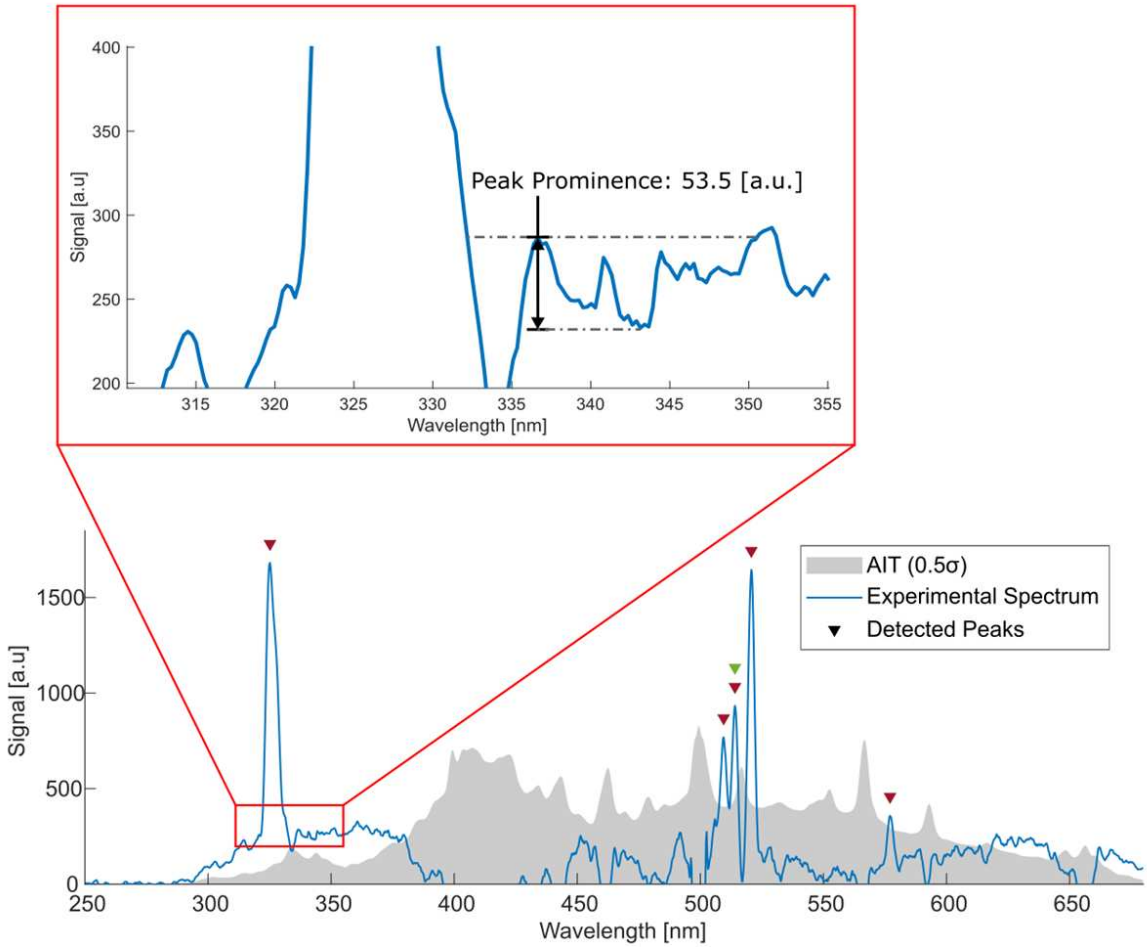

Figure 4.3: Example calculation of peak prominence for an experimental LIBS spectrum after air subtraction.

The example LIBS signal in Figure 4.3 illustrates the importance of using a prominence threshold in addition to the AIT. Residual spectral noise following air subtraction is present in this signal

exceeding the AIT in the range of ~300-400nm. The noise peak at 335.2 nm for which the prominence is calculated in Figure 4.3 exists within the detection window centered on 334.9 nm (corresponding to titanium emission). Therefore, if the PT value were less than 53.5, this peak would be detected and contribute to the Material Score for titanium. In this example, however, the Material Score of the correct class (copper) is 5, meaning an additional erroneous titanium peak identification would not influence the final classification assigned by the algorithm.

Rather than examine the effects of varying the PT on algorithm performance, a constant value of 60 (arbitrary intensity counts) was selected and used for all analysis. To select the optimal value of PT, we plot the macro-averaged F1 score over AIT = [0,1σ] for a range of prominence thresholds. Each line in Figure 4.4 represents a different (constant) PT from 0 to 140 in increments of 20. The maximum average F1 score was achieved at a prominence threshold of 60 counts [a.u]. For each test spectrum, a Material Score (M) is assigned for each class based on the number of positively identified peaks associated with the class and can range from 0-5 for each candidate material. Final assignment logic can be adjusted depending on the application but for initial work the classifier assumes each test particle belongs to only one class based on the maximum Material Score and with a requirement of a minimum usable Material Score of 2. If the maximum material score is not met (i.e., fewer than 2 peaks detected for any individual material class), the signal is considered to be an air-only spectrum. An example experimental spectrum in Figure 4.5 contains five peaks identified as titanium. The strong peak located at ~324 nm was also recorded toward the material score for copper, due to overlap of detection windows. Material scores for the example spectrum in Figure 4.5 are therefore $M_{Ti} = 5$ and $M_{Cu} = 1$, resulting in a correct classification of titanium.

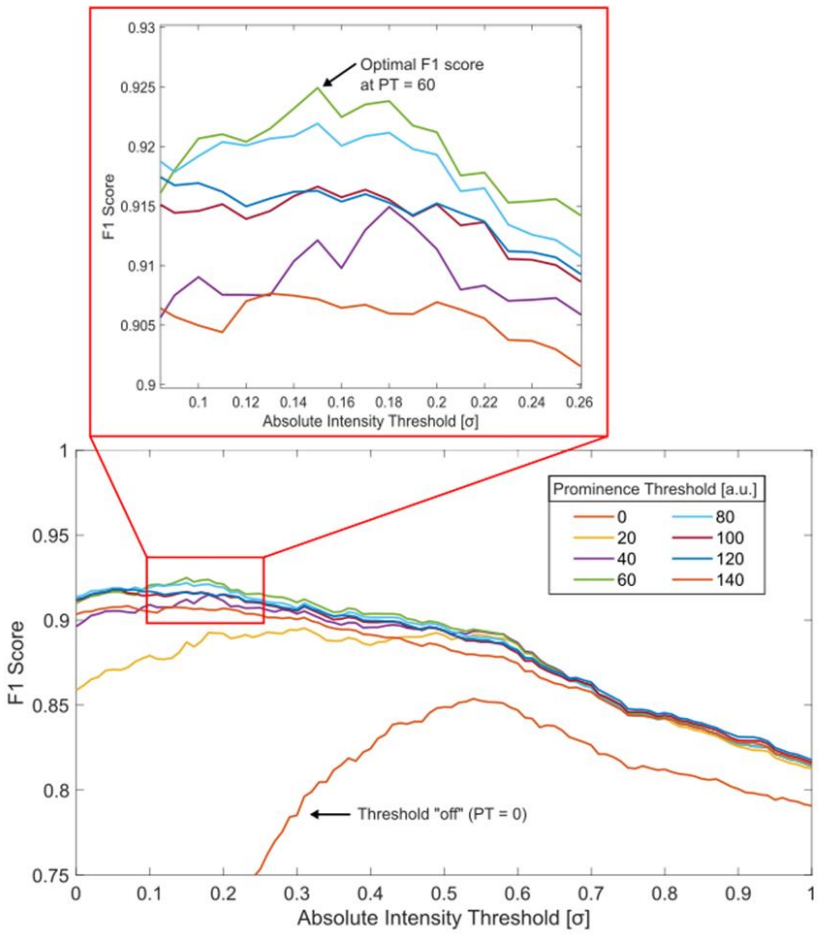

Figure 4.4: Macro-averaged F1 score vs AIT for prominence threshold values 0 to 140.

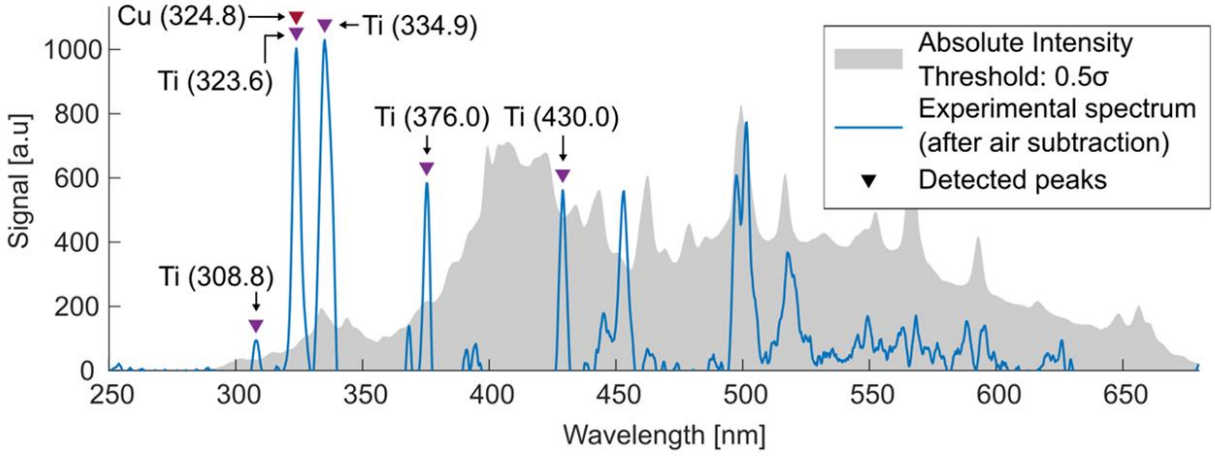

Figure 4.5: Example LIBS spectrum containing emission from a titanium particle after air subtraction. The gray shaded region indicates an Absolute Intensity Threshold (AIT) value of 0.5σ that must be exceeded for a positive peak detection. Detected peaks and their corresponding material class are identified with triangular markers.

The current implementation of the algorithm requires the classifier to select a single class for each signal. In the rare cases (<5%) in which the resulting Material Scores for multiple classes are equal, the class with the highest mean peak intensity is selected. The classifier identification was performed as a post-processing step for the initial work but could be implemented into real-time data analysis in the future.

4.1.3 Classifier performance metrics

To examine the performance of our Classifier Algorithm, we compare the predictions of material class against the manual (truth) classifications for the set of 1480 test spectra. The algorithmic approach can be treated as a multiclass problem based on assigning test spectra to respective classes corresponding to material, including air-only. The class counts obtained by the algorithm and by manual classification are used to calculate quality metrics of True Positive Rate (TPR), Precision, and False Positive Rate (FPR):

$$TPR = \frac{TP}{TP+FN} \qquad Precision = \frac{TP}{TP+FP} \qquad FPR = \frac{FP}{FP+TN} \qquad (4.1a, b, c)$$

where *TP* and *TN* are the number of true positives and true negatives, *FP* is the number of false positives (type I error), and *FN* is the number of false negatives (type II error). Applying this formalism to multi-class problems is done using a one-versus-all approach[71], such that analyses are performed on a given material class (e.g., the material type of copper) and against all remaining classes. For example, assigning a true copper signal as titanium would be a false positive in analysis of the titanium class, a false negative when considering the copper class, and a true negative when calculating any other class. As shown below, achievable values of these parameters vary with the logic and threshold settings and required values of TPR, precision, and FPR will vary with application. For example, for safety alarms due to possible high-risk materials it may be

acceptable to have more false positives in order to not miss any true positives, i.e., to tolerate a higher FPR to achieve a high TPR. Alternatively, in a case where each positive triggers a high-cost action (e.g., expensive follow-on testing or an equipment shutdown), it may be important that any positive assignments have a high probability of being correct, corresponding to need for high Precision. Without additional knowledge of the relative importance of TPR and Precision, a useful performance metric is the F_1 score. The F_1 score provides a measure of the overall agreement between truth and algorithmic classifications, with equal weighting given to both Precision and *TPR* and is calculated with Eqn. (4.2)[72]:

$$F_1 = 2 * \frac{Precision * TPR}{Precision + TPR} = \frac{TP}{TP + \frac{1}{2}(FP + FN)} \tag{4.2}$$

Higher values of F_1 indicate better performance (with a range from 0 to 1).

An additional performance metric, which also accounts for the instrument flow configuration and plasma overlap, is provided by the LIBS Efficiency (η_{LIBS}) defined as the fraction of particles entering the DRPS (through the 1.5 mm inlet) that are correctly identified:

$$\eta_{LIBS} = \frac{\#\ of\ correctly\ identified\ particles}{\#\ of\ particles\ detected\ by\ trigger\ beam} \tag{4.3}$$

Where "correctly identified particles" indicates agreement between the automated and truth signal classifications excluding the air-only class and "particles detected" considers only particles large enough to generate a LIBS trigger signal. A high LIBS efficiency means a higher fraction of detectable particles entering the DRPS will be correctly classified by material. Cases where spectra are misclassified by the algorithm or cases where the LIBS microplasma misses the particle both reduce η_{LIBS}. Therefore, even if the algorithm were to classify all spectra with perfect accuracy,

the peak value of LIBS efficiency is limited by the probability of the microplasma successfully hitting a falling particle which is in the range of 50-60% for most tested particle types.

4.2 LIBS signal classifier results

The classification algorithm was applied to the test dataset using different values of the absolute intensity threshold (AIT) ranging from 0 to 1σ. Figure 4.6 shows plots of TPR, FPR, Precision and the F_1 score for one-versus-all analyses based on each material class (and their macro-averaged values) versus AIT. Each of these parameters can range from 0 to 1, with high values indicating better performance, except in the case of FPR where low values are preferred. With regards to TPR (for non-air materials), the general trend is simply that increasing the AIT much above zero causes the TPR rate to start to fall – this can be interpreted that, as thresholds get larger, it is increasingly likely for the algorithm to miss weak spectral emissions. However, there can be a penalty for too low of a threshold, in that the algorithm can mistakenly consider noise (or subtraction artifacts) as actual material peaks, i.e., there will be false positive. For this reason, we see that if the AIT is very low (<~ 0.15σ), we have a decrease in Precision and an increase in FPR.

The F_1 parameter describes the combination of TPR and Precision and for most material classes is highest when the intensity threshold is in the range of ~0.15σ. Intuitively it is reasonable that some minimum threshold is helpful to reject noise artifacts but that too large of a threshold lowers performance since the system becomes blind to actual emission lines. The exact performance varies for different materials (likely due to the locations and strengths of the target lines relative to air plasma lines and spectral regions with more fluctuation) but we can achieve $F_1 \geq 0.9$ for all classes. The differing behavior for silver-coated glass where higher AIT values remain adequate is likely because the silver peaks tend to be very strong and easier to differentiate from any baseline noise. Clearly, a different optimal threshold value may exist for other materials. However, three of

the four studied test materials display roughly the same relationship between F_1 score and AIT. Thus, statistics based on the macro-averaged case are assumed to be the most appropriate when selecting an operating point for the classification of other materials. If high confidence in positive identifications is required, the optimal value of AIT (~0.6σ) occurs when Precision is maximized.

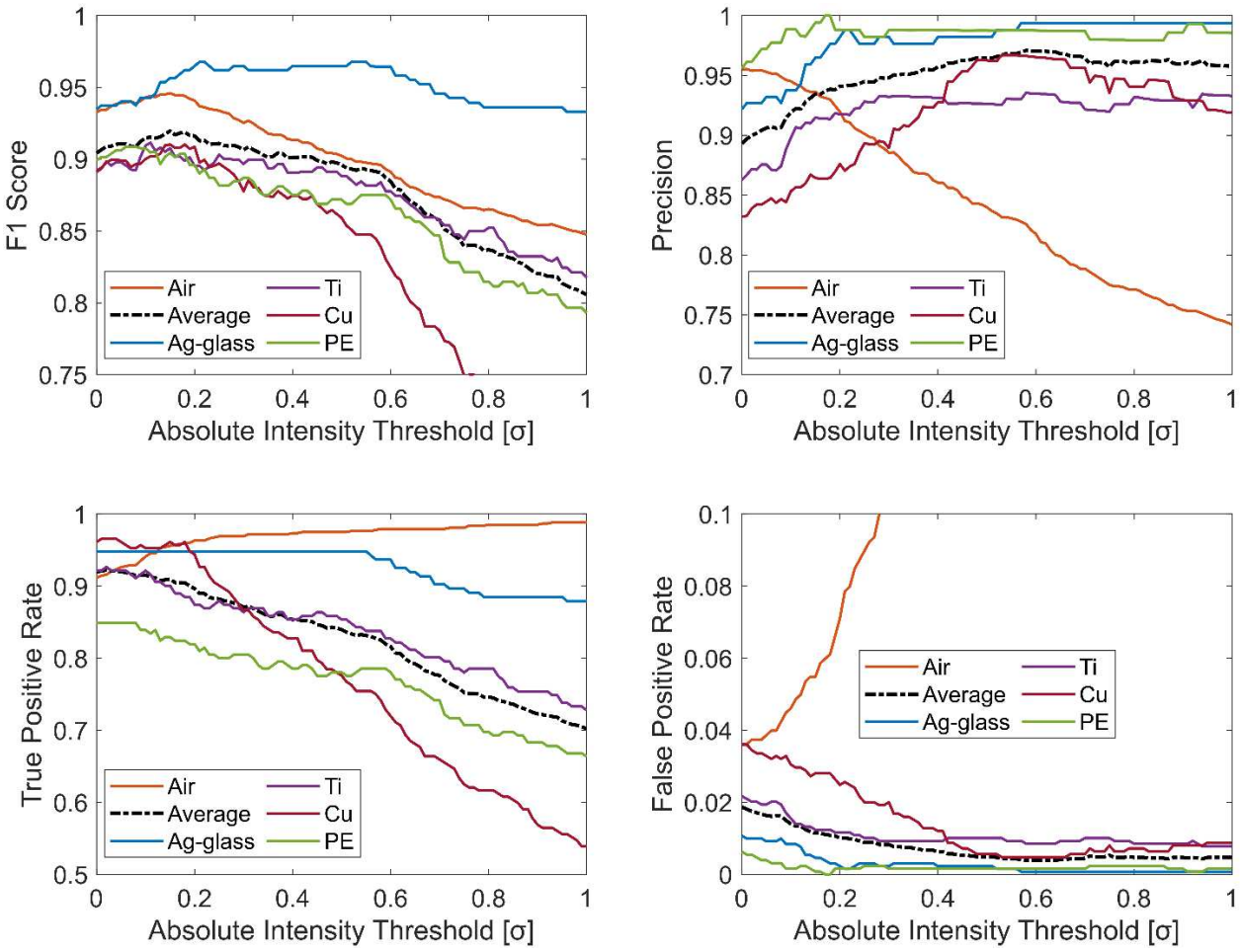

Figure 4.6: F_1 score, Precision, TPR, and FPR for each test particle class, macro-average of the four classes (dashed line), and air-only spectra over $0 \leq AIT \leq 1$.

Table 4.1: Classifier performance statistics for three representative values of Absolute Intensity Threshold: AIT = 0 (threshold off), AIT = 0.15σ (maximum F_1 score), and AIT = 0.6σ (maximum Precision).

AIT [σ]	# Correct	TPR	FPR	Precision	F_1	η_{LIBS}
0	1356	0.92	0.019	0.89	0.90	0.53
0.15	1378	0.91	0.011	0.94	0.92	0.53
0.6	1320	0.83	0.004	0.97	0.89	0.48

4.3 Efficiency & optimization

Regarding LIBS efficiency, we find values of ~0.48-0.53 for AIT between 0.15σ and 0.6σ, driven primarily by the hit rate of particles. This means that a LIBS signal usable for particle classification could be obtained for roughly half of all the detectable particles that entered the DRPS and transited both scattering beams. Because a particle must transit the lower scattering beam in order to trigger the LIBS pulse, it can be assumed that the particle in question generated a signal pair necessary to make an aerodynamic diameter measurement in addition to the composition information obtained from the LIBS signal.

While the results of the present work are already quite promising for practical use, various modifications to increase performance can be considered for optimization in future work. Detection efficiencies achieved by the prototype LIBS system of approximately 50% would provide useful information about the composition of airborne particles in a sample environment, but there remain some limitations and areas for possible optimization. The LIBS efficiency is driven by two major factors—the probability of the plasma successfully ablating a particle (aerosol hit rate) and the classification accuracy of the peak detection algorithm.

The accuracy of the classifier can be improved by algorithmic changes (e.g., details of the air plasma subtraction step), hardware changes in relation to spectral acquisition, or reduction of the total material classes considered by the algorithm for a given signal. The air plasma subtraction methodology is an important area of optimization for the current implementation of the LIBS spectrum classifier. If the spectral contribution to the raw LIBS signal from the ambient air and continuum emission can be completely removed, the only remaining features will be emission peaks from aerosol material ablated by the plasma. However, variability in the intensity and shape of the air and continuum features between laser shots makes this difficult to achieve. The characteristics of the plasma are influenced by environmental factors such as air temperature, pressure, and the concentration of small ambient aerosols. One such way to improve the air plasma subtraction step is to use a higher resolution and/or time-gated spectrometer. Higher spectral resolution would make the emission peaks from both the air and analyte narrower and easier to distinguish from one another. Narrower peaks would allow the exclusion windows used to avoid particle emission during air subtraction to be smaller. The use of a time-gated spectrometer detector would allow spectral acquisition to begin a few microseconds after initiation of the plasma, when continuum emission is much less intense. Any improvements to the air plasma subtraction would increase the signal-to-noise ratio after air subtraction and make aerosol composition classification easier.

One limitation of the current material classification algorithm is that the possible materials and their corresponding emission wavelengths must be specified beforehand. These wavelengths can be based on a spectroscopic database to detect the presence of a specific element or compound in the sample. However, for applications in which multi-element particles are distinguished from one another (e.g., source apportionment), the wavelengths of interest must be determined

experimentally via LIBS analysis prior to automated detection using the DRPS. Furthermore, the classification accuracy of the algorithm is reduced as more materials are added to the list of possible material classes. The primary reason for this is the air plasma feature and continuum emission removal methodology. Spectral regions where non-air emission peaks can be expected are excluded when fitting a representative air spectrum for subtraction. As more points are excluded from the spectra, accuracy of the least squares regression matching decreases, resulting in a noisier LIBS signal after air subtraction. For example, there are 4 materials (silver-coated glass, copper, titanium, and polyethylene) used in this in this work for a total of 20 emission wavelengths of interest. The exclusion region for each peak is 24 detector pixels (6 nm) wide—roughly the width at the base of a strong emission peak. This means a maximum of 480 of 1671 total data points are excluded when performing the least squares fit (in practice, this number is lower due to the overlap of zones). If, for example, a fifth material were added to the possible classifications, an additional 120 data points would be removed. This also means that the classification algorithm would likely perform better in a use case where a smaller number of particle types need to be identified. An example of the simplest case is monitoring for the presence of a single particle type (i.e. a toxic species or aerosols from a specific source). In this case, the algorithm need only make a binary decision which is less prone to misclassification.

An increased aerosol hit rate may be achieved through alternative beam-focusing optics or adjustment of the plasma/inlet geometry. Changes to the DRPS hardware to increase the aerosol hit rate including reduction of the inlet diameter and higher laser pulse energy have been investigated with a maximum reliable hit rate achieved across all particle types and sizes of 40-60%. Additional modifications, such as an aerosol-focusing sheath air flow or increasing the size

of the plasma kernel with different focusing optics have been proposed but not implemented or tested.

CHAPTER 5 – CONCLUSIONS & FUTURE WORK

The prototype DRPS sampler was able to provide accurate single-particle measurements of aerodynamic diameter using a time-of-flight calculation over the 25-125 µm range when evaluated with spherical particles in laboratory conditions. The LIBS system was successfully integrated into the prototype DRPS without compromising the time-of-flight measurement as a step toward simultaneous real time counting/sizing and elemental composition of large inhalable particles. We have developed an automated analysis method able to correctly classify a large majority of test spectra from four particle types. The method includes subtracting contributions (matrix effects) from the air plasma emission contribution and using a thresholding approach to identify features against a prepopulated spectral database. The effect of the intensity threshold on classifier performance metrics including F_1 score and Precision was examined and revealed potential operating points.

Although the results of the present work are promising, additional modifications to increase performance should be considered in the future. The primary improvement methods identified during the current work are 1) the reduction of transmission losses (detectable particles that enter the device but do not transit both scattering beams) and increasing LIBS efficiency, which is related to the particle hit rate. The potential benefits of reducing the vertical separation of the two scattering beams and the effect of the inlet orifice diameter were examined in section 3.3. The analysis of beam separation and inlet geometry in this work could provide insight to improve the design of the next iteration of the DRPS prototype. In addition to increasing the allowable ambient particle concentration before coincidence error is encountered, a reduction in the distance a particle

must travel between particle detection stages would decrease the probability of particles depositing within the device between scattering beams and therefore reduce transmission losses. The LIBS efficiency is driven by two major factors—the probability of the plasma successfully ablating a particle (aerosol hit rate) and the classification accuracy of the peak detection algorithm. An increased aerosol hit rate may be achieved through alternative beam-focusing optics or adjustment of the plasma/inlet geometry. The accuracy of the classifier can be improved by algorithmic changes (e.g., details of the air plasma subtraction step) or changes spectral acquisition hardware. Machine learning approaches, including principal component analysis, support vector regression, and artificial neural networks[73] have also been demonstrated for LIBS data processing for identification of materials with similar elemental composition (e.g., polymers[74] and soils[75]) and can be examined in future work to extend the capabilities of the DRPS. The next step in the development of the DRPS may be to deploy the instrument in the field to study the measurement accuracy on real aerosol distributions rather than those generated in the laboratory under known conditions. The ability of the DRPS to directly measure the aerodynamic diameter and characterize particle composition in near real time is potentially valuable for occupational hazard identification, industrial process monitoring, and many other fields of aerosol research.

REFERENCES

1. Phalen R, Hinds W, John W, et al. *PARTICLE SIZE-SELECTIVE SAMPLING IN THE WORKPLACE: RATIONALE AND RECOMMENDED TECHNIQUES*. Vol 32.; 1988.

2. Davidson CI, Phalen RF, Solomon PA. Airborne particulate matter and human health: A review. *Aerosol Science and Technology*. 2005;39(8):737-749. doi:10.1080/02786820500191348

3. Linnainmaa M, Laitinen J, Leskinen A, Sippula O, Kalliokoski P. Laboratory and field testing of sampling methods for inhalable and respirable dust. *J Occup Environ Hyg*. 2008;5(1):28-35. doi:10.1080/15459620701763723

4. Brown JS, Gordon T, Price O, Asgharian B. Thoracic and respirable particle definitions for human health risk assessment. *Part Fibre Toxicol*. 2013;10(1):1-12. doi:10.1186/1743-8977-10-12

5. ISO. Particle Size Fraction Definitions for Health-Related Sampling. ISO 7708:1995. Published 1995. https://www.iso.org/obp/ui/#iso:std:iso:7708:en

6. Volkwein JC, Maynard AD, Harper M. Workplace Aerosol Measurement. *Aerosol Measurement: Principles, Techniques, and Applications: Third Edition*. Published online 2011:571-590. doi:10.1002/9781118001684.ch25

7. Cheng YS, Zhou Y, Chen BT. Particle deposition in a cast of human oral airways. *Aerosol Science and Technology*. 1999;31(4):286-300. doi:10.1080/027868299304165

8. Salvaggio JE. Inhaled particles and respiratory disease. *J Allergy Clin Immunol*. 1994;94(2 SUPPL. 18):304-309. doi:10.1053/ai.1994.v94.a56009

9. Youlden DR, Cramb SM, Peters S, et al. International comparisons of the incidence and mortality of sinonasal cancer. *Cancer Epidemiol*. 2013;37(6):770-779. doi:10.1016/j.canep.2013.09.014

10. de Vocht F, Sobala W, Wilczynska U, Kromhout H, Szeszenia-Dabrowska N, Peplonska B. Cancer mortality and occupational exposure to aromatic amines and inhalable aerosols in rubber tire manufacturing in Poland. *Cancer Epidemiol*. 2009;33(2):94-102. doi:10.1016/j.canep.2009.06.013

11. Li K, Aghazadeh F, Hatipkarasulu S, Ray TG. Health risks from exposure to metal-working fluids in machining and grinding operations. *International Journal of Occupational Safety and Ergonomics*. 2003;9(1):75-95. doi:10.1080/10803548.2003.11076555

12. OSHA. Permissible Exposure Limits (PELs). Published 2005. http://www.osha.gov/SLTC/pel/

13. Belyaev SP, Levin LM. *TECHNIQUES FOR COLLECTION OF REPRESENTATIVE AEROSOL SAMPLES*. Vol 5. Pergamon Press

14. Su YY, Li ZM, Li M, et al. Development of aerosol sample introduction interface coupled with ICP-MS for direct introduction and quantitative online monitoring of environmental aerosol. *Aerosol Science and Technology*. 2014;48(1):99-107. doi:10.1080/02786826.2013.861894

15. Wilschefski S, Baxter M. Inductively Coupled Plasma Mass Spectrometry: Introduction to Analytical Aspects. *Clinical Biochemist Reviews*. 2019;40(3):115-133. doi:10.33176/aacb-19-00024

16. Jayne JT, Leard DC, Zhang X, et al. Development of an aerosol mass spectrometer for size and composition analysis of submicron particles. *Aerosol Science and Technology*. 2000;33(1-2):49-70. doi:10.1080/027868200410840

17. Volckens J, Peters TM. Counting and particle transmission efficiency of the aerodynamic particle sizer. *J Aerosol Sci*. 2005;36(12):1400-1408. doi:10.1016/j.jaerosci.2005.03.009

18. Heim M, Mullins BJ, Umhauer H, Kasper G. Performance evaluation of three optical particle counters with an efficient "multimodal" calibration method. *J Aerosol Sci*. 2008;39(12):1019-1031. doi:10.1016/j.jaerosci.2008.07.006

19. Pinnick RG, Rosen JM, Hofmann DJ. Measured Light-Scattering Properties of Individual Aerosol Particles Compared to Mie Scattering Theory. *Appl Opt*. 1973;12(1):37. doi:10.1364/ao.12.000037

20. Howard M, Luttman A, Operations N, et al. *Mie Scattering Analysis New Mexico Operations with Contributions From*.; 2016.

21. Jackson JD, Levitt LC. Classical Electrodynamics. *Phys Today*. 1962;15(11):62-62. doi:10.1063/1.3057859

22. Liu BYH, Berglund RN, Agarwal JK. *EXPERIMENTAL STUDIES OF OPTICAL PARTICLE COUNTERS*. Vol 8. Pergamon Press; 1974.

23. Hinds WC. *Aerosol Technology: Properties, Behavior, and Measurement of Airborne Particles*. 2nd ed. Wiley; 1999.

24. Szymanski WW, Nagy A, Czitrovszky A. Optical particle spectrometry-Problems and prospects. *J Quant Spectrosc Radiat Transf*. 2009;110(11):918-929. doi:10.1016/j.jqsrt.2009.02.024

25. Chien CH, Theodore A, Wu CY, Hsu YM, Birky B. Upon correlating diameters measured by optical particle counters and aerodynamic particle sizers. *J Aerosol Sci*. 2016;101:77-85. doi:10.1016/j.jaerosci.2016.05.011

26. Czitrovszky A. Environmental applications of solid-state lasers. In: *Handbook of Solid-State Lasers: Materials, Systems and Applications*. Elsevier Ltd; 2013:616-646. doi:10.1533/9780857097507.2.616

27. Jaenicke R. *THE OPTICAL PARTICLE COUNTER: CROSS-SENSITIVITY AND COINCIDENCE*. Vol 30. Pergamon Press; 1972.

28. Hidy GM. Aerosols. In: Meyers RA, ed. *Encyclopedia of Physical Science and Technology (Third Edition)*. Third Edition. Academic Press; 2003:273-299. doi:https://doi.org/10.1016/B0-12-227410-5/00014-4

29. Anderson KR, Leith D, Ndonga M, Volckens J. Novel instrument to separate large inhalable particles. *Aerosol Science and Technology*. 2015;49(12):1195-1209. doi:10.1080/02786826.2015.1112874

30. DeCarlo PF, Slowik JG, Worsnop DR, Davidovits P, Jimenez JL. Particle morphology and density characterization by combined mobility and aerodynamic diameter measurements. Part 1: Theory. *Aerosol Science and Technology*. 2004;38(12):1185-1205. doi:10.1080/027868290903907

31. Carranza JE, Fisher BT, Yoder GD, Hahn DW. On-line analysis of ambient air aerosols using laser-induced breakdown spectroscopy. *Spectrochim Acta Part B At Spectrosc*. 2001;56(6):851-864. doi:10.1016/S0584-8547(01)00183-5

32. Kim G, Kim K, Maeng H, Lee H, Park K. Development of aerosol-LIBS (Laser induced breakdown spectroscopy) for real-time monitoring of process-induced particles. *Aerosol Air Qual Res*. 2019;19(3):455-460. doi:10.4209/aaqr.2018.08.0312

33. Xiong G, Li S, Zhang Y, Buckley SG, Stephen DT. Phase-selective laser-induced breakdown spectroscopy of metal-oxide nanoparticle aerosols with secondary resonant excitation during flame synthesis. *J Anal At Spectrom*. 2016;31(2):482-491.

34. Cremers DA, Radziemski LJ. *Handbook of Laser-Induced Breakdown Spectroscopy*. 2nd ed. John Wiley & Sons, Ltd.; 2013.

35. Fortes FJ, Fernández-Bravo A, Javier Laserna J. Chemical characterization of single micro- and nano-particles by optical catapulting-optical trapping-laser-induced breakdown spectroscopy. *Spectrochim Acta Part B At Spectrosc*. 2014;100:78-85. doi:10.1016/j.sab.2014.08.023

36. Kumar AU, Leonov BS, Wu Y, Limbach C. Spatio-temporal studies on laser induced plasma interactions with micro-particles using stereo-imaging. In: *AIAA Scitech 2021*

Forum. AIAA SciTech Forum. American Institute of Aeronautics and Astronautics; 2021. doi:doi:10.2514/6.2021-1376

37. Hymer CB', Caruso JA. *Nebulizer Sample Introduction for Elemental Speciation*.; 2000.

38. Vadillo JM, Laserna JJ. Laser-induced plasma spectrometry: Truly a surface analytical tool. *Spectrochim Acta Part B At Spectrosc*. 2004;59(2):147-161. doi:10.1016/j.sab.2003.11.006

39. Borduchi LCL, Milori DMBP, Villas-Boas PR. Study of the effects of detection times in laser-induced breakdown spectroscopy and missed variation of plasma parameters with gate width. *Spectrochim Acta Part B At Spectrosc*. 2022;191. doi:10.1016/j.sab.2022.106409

40. Bilge G, Eseller KE, Berberoglu H, Sezer B, Tamer U, Boyaci IH. Comparison of different calibration techniques of laser induced breakdown spectroscopy in bakery products: on NaCl measurement. *Journal of the European Optical Society-Rapid Publications*. 2021;17(1). doi:10.1186/s41476-021-00164-9

41. Kramida A, Olsen K, Ralchenko Y. NIST LIBS Database. National Institute of Standards and Technology (NIST). Published 2019. https://physics.nist.gov/PhysRefData/ASD/LIBS/libs-form.html

42. Ji H, Ding Y, Zhang L, Hu Y, Zhong X. Review of aerosol analysis by laser-induced breakdown spectroscopy. *Appl Spectrosc Rev*. 2021;56(3):193-220. doi:10.1080/05704928.2020.1780604

43. Lithgow GA, Buckley SG, Lithgow G, Buckley S, Buckley SG. *Influence of Particle Location Within Plasma and Focal Volume on Precision of Single-Particle LIBS Measurements*.; 2005.

44. Carranza JE, Hahn DW. Assessment of the upper particle size limit for quantitative analysis of aerosols using laser-induced breakdown spectroscopy. *Anal Chem*. 2002;74(21):5450-5454. doi:10.1021/ac020261m

45. Stipe CB, Miller AL, Brown J, Guevara E, Cauda E. Evaluation of laser-induced breakdown spectroscopy (LIBS) for measurement of silica on filter samples of coal dust. *Appl Spectrosc*. 2012;66(11):1286-1293. doi:10.1366/12-06671

46. Watson JG, Zhu T, Chow JC, Engelbrecht J, Fujita EM, Wilson WE. *Receptor Modeling Application Framework for Particle Source Apportionment*. www.elsevier.com/locate/chemosphere

47. Kebe M, Traore A, Manousakas MI, et al. Source apportionment and assessment of air quality index of pm2.5–10 and pm2.5 in at two different sites in urban background area in senegal. *Atmosphere (Basel)*. 2021;12(2):1-16. doi:10.3390/atmos12020182

48. Panne U, Neuhauser RE, Theisen M, Fink H, Niessner R. Analysis of heavy metal aerosols on filters by laser-induced plasma spectroscopy. *Spectrochim Acta Part B At Spectrosc*. 2001;56(6):839-850. doi:10.1016/S0584-8547(01)00209-9

49. Diwakar P, Kulkarni P, Birch ME. New approach for near-real-time measurement of elemental composition of aerosol using laser-induced breakdown spectroscopy. *Aerosol Science and Technology*. 2012;46(3):316-332. doi:10.1080/02786826.2011.625059

50. Heikkilä P, Rossi J, Rostedt A, et al. Toward elemental analysis of ambient single particles using electrodynamic balance and laser-induced breakdown spectroscopy. *Aerosol Science and Technology*. 2020;54(7):837-848. doi:10.1080/02786826.2020.1727408

51. Järvinen ST, Toivonen J. Analysis of single mass-regulated particles in precisely controlled trap using laser-induced breakdown spectroscopy. *Opt Express*. 2016;24(2):1314. doi:10.1364/oe.24.001314

52. Hahn DW, Lunden MM. Detection and analysis of aerosol particles by laser-induced breakdown spectroscopy. *Aerosol Science and Technology*. 2000;33(1-2):30-48. doi:10.1080/027868200410831

53. Lithgow GA, Buckley SG, Lithgow G, Buckley S, Buckley SG. *Influence of Particle Location Within Plasma and Focal Volume on Precision of Single-Particle LIBS Measurements*.; 2005.

54. Tjärnhage T, Gradmark P, Larsson A, et al. Development of a laser-induced breakdown spectroscopy instrument for detection and classification of single-particle aerosols in real-time. *Opt Commun*. 2013;296:106-108. doi:10.1016/j.optcom.2013.01.044

55. Stipe CB, Miller AL, Brown J, Guevara E, Cauda E. Evaluation of laser-induced breakdown spectroscopy (LIBS) for measurement of silica on filter samples of coal dust. *Appl Spectrosc*. 2012;66(11):1286-1293. doi:10.1366/12-06671

56. Radziemski LJ, Loree TR, Cremers DA, Hoffman NM. *Time-Resolved Laser-Induced Breakdown Spectrometry of Aerosols The Classic Method for Generating a Laser Spark*. Vol 55.; 1983. https://pubs.acs.org/sharingguidelines

57. Carranza JE, Iida K, Hahn DW. Conditional data processing for single-shot spectral analysis by use of laser-induced breakdown spectroscopy. *Appl Opt*. 2003;42(30):6022. doi:10.1364/ao.42.006022

58. Carranza JE, Fisher BT, Yoder GD, Hahn DW. *On-Line Analysis of Ambient Air Aerosols Using Laser-Induced Breakdown Spectroscopy*. Vol 56.; 2001.

59. Álvarez-Trujillo LA, Ferrero A, Laserna JJ, Hahn DW. Alternative Statistical Methods for Spectral Data Processing: Applications to Laser-Induced Breakdown Spectroscopy of

Gaseous and Aerosol Systems. *Appl Spectrosc*. 2008;62(10):1144-1152. doi:10.1366/000370208786049178

60. Yao S, Zhang L, Yin K, et al. Identifying laser-induced plasma emission spectra of particles in a gas-solid flow based on the standard deviation of intensity across an emission line. *J Anal At Spectrom*. 2018;33(10):1676-1682. doi:10.1039/c8ja00194d

61. Zheng J, Lu J, Zhang B, et al. Experimental study of laser-induced breakdown spectroscopy (LIBS) for direct analysis of coal particle flow. *Appl Spectrosc*. 2014;68(6):672-679. doi:10.1366/13-07278

62. Sipich J, L'Orange C, Anderson K, Limbach C, Volckens J, Yalin A. A direct-reading particle sizer with elemental composition analysis for large inhalable particles. *Aerosol Science and Technology*. 2022;56(3):223-233. doi:10.1080/02786826.2021.2002255

63. Sipich J, L'Orange C, Volckens J, Yalin A. In-Situ Elemental Composition Analysis of Large Inhalable Aerosol Using Laser Induced Breakdown Spectroscopy. *Appl Spectrosc*. Published online December 6, 2022:00037028221146804. doi:10.1177/00037028221146804

64. Alberti A, Munafo A, Koll M, et al. Laser-induced non-equilibrium plasma kernel dynamics. *J Phys D Appl Phys*. 2020;53(2). doi:10.1088/1361-6463/ab492a

65. Brieschenk S, Kleine H, Obyrne S. The effect of blast wave re-focusing on a laser-induced plasma. *J Appl Phys*. 2013;113(10). doi:10.1063/1.4794017

66. Harmon RS, Russo RE. Laser-Induced Breakdown Spectroscopy. *Treatise on Geochemistry: Second Edition*. 2013;15(October):245-272. doi:10.1016/B978-0-08-095975-7.01417-0

67. Schneider CA, Rasband WS, Eliceiri KW. NIH Image to ImageJ: 25 years of image analysis. *Nat Methods*. 2012;9(7):671-675. doi:10.1038/nmeth.2089

68. Lehnert M, Pesch B, Lotz A, et al. Exposure to inhalable, respirable, and ultrafine particles in welding fume. *Annals of Occupational Hygiene*. 2012;56(5):557-567. doi:10.1093/annhyg/mes025

69. Lin CC, Chen MR, Chang SL, Liao WH, Chen HL. Characterization of ambient particles size in workplace of manufacturing physical ftness equipments. *Ind Health*. 2015;53(1):78-84. doi:10.2486/indhealth.2014-0160

70. Baldwin PEJ, Maynard AD. A Survey of Wind Speeds in Indoor Workplaces. *Ann Occup Hyg*. 1998;(August). doi:10.1093/annhyg/42.5.303

71. Rifkin R, Klautau A. In Defense of One-Vs-All Classification. *Journal of Machine Learning Research*. 2004;5:101-141.

72. Chinchor N. *MUC-4 Evaluation Metrics, in Proc. of the Fourth Message Understanding Conference*.; 1992.

73. Gonçalves DA, Senesi GS, Nicolodelli G. Laser-Induced Breakdown Spectroscopy applied to environmental systems and their potential contaminants. An overview of advances achieved in the last few years. *Trends in Environmental Analytical Chemistry*. 2021;30. doi:10.1016/j.teac.2021.e00121

74. Boueri M, Motto-Ros V, Lei WQ, et al. Identification of Polymer Materials Using Laser-Induced Breakdown Spectroscopy Combined with Artificial Neural Networks. *Appl Spectrosc*. 2011;65(3):307-314. doi:10.1366/10-06079a

75. el Haddad J, Villot-Kadri M, Ismaël A, et al. Artificial neural network for on-site quantitative analysis of soils using laser induced breakdown spectroscopy. *Spectrochim Acta Part B At Spectrosc*. 2013;79-80:51-57. doi:10.1016/j.sab.2012.11.007